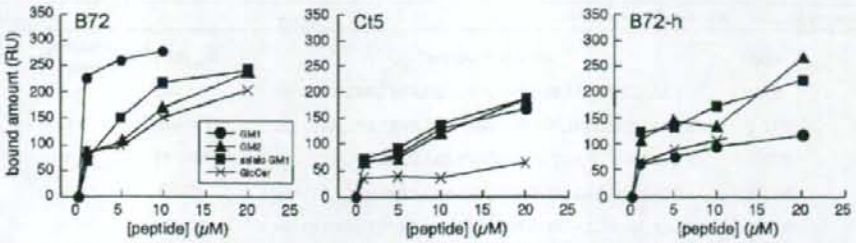

FIGURE 6: Amounts of B72, Ct5, and B72-h peptides bound to gangliosides and GSLs observed by SPR spectroscopy.

Table 2: Affinity of Synthetic Peptides for GM1, GM2, Asialo GM1, and GlcCer

peptide	glycolipid	R_{max} (RU)	K_d (μM)	relative affinity[a]
B72	GM1	280	0.24	1.0
	GM2	418	15	0.016
	asialo GM1	278	3.3	0.073
	GlcCer	322	12	0.020
Ct5	GM1	268	11	1.0
	GM2	377	21	0.52
	asialo GM1	275	9.9	1.1
	GlcCer	nd[b]	nd[b]	nd[b]
B72-h	GM1	145	5.0	1.0
	GM2	274	2.1	2.4
	asialo GM1	285	5.9	0.85
	GlcCer	110	0.77	6.5

[a] Ratio to GM1. [b] Not detectable.

therefore designed a novel carbohydrate-binding peptide with a structural scaffold in this study.

A helical conformation is the only structure that we can design. A helix−loop−helix (or helix−turn−helix) scaffold allows a peptide to form a stable helical structure. Fujii et al. designed a helix−loop−helix peptide library; the helix outside of five residues at 24, 25, 28, 31, and 32 was randomized to give a peptide library (*31*). The N-terminal residues interact with the C-terminus to stabilize the α-helical structure; therefore, this peptide is a monomer and does not form a dimer. They previously identified peptide agonists of the cytokine receptor and granulocyte colony-stimulating factor receptor using helix−loop−helix libraries (unpublished data). In this study, we conferred the ability to recognize carbohydrates on this peptide. The selection procedure followed that previously reported by us; a glycolipid monolayer was immobilized onto a plate and incubated with the phage library (*25*). This method allows the suppression of nonspecific interaction of phage particles with the lipid portion of the glycolipid and the plate surface exposed. The phage particles therefore interact with only the exposed carbohydrate portion of the glycolipid. The two GM1-positive clones, A914 and B72, were identified via a phage ELISA and were chemically synthesized. A synthetic B72 peptide showed specific binding to GM1 with a K_d of 0.24 μM and was found to have the highest affinity for GM1 as suggested by the phage ELISA (Table 1). The K_d value of Ct5, as a control peptide, was 11 μM, and Ct5 exhibited no specificity (Table 2 and Figure 6). This is because the helix−loop−helix scaffold contains several charged amino acids, glutamic acids (positions 2, 7, 9, and 14), and lysines (positions 22, 27, 29, and 34). These amino acids are able to interact nonspecifically with carbohydrates through hydrogen binding and/or salt bridges. These nonspecific interactions contributed to the binding affinity but were not involved directly in the specific interaction between the peptide and GM1 oligosaccharide. Therefore, the five amino acids, Lys24, Ala25, Arg28, Arg31, and Phe31, would be very important for the specific recognition of GM1. Furthermore, to determine whether formation of a helix is essential for binding, we designed a B72-h peptide that is the 18 C-terminal residues containing the five amino acids. The CD spectrum of B72-h exhibited an unordered structure (Figure 5). The five amino acid residues are therefore randomly arranged, and the orientation of these side chains would not be restricted. As expected, B72-h lost affinity and selectivity for GM1 (K_d = 5.0 μM) (Table 2 and Figure 6). These results indicate that the helical conformation of B72 is essential for the recognition of GM1.

Next, alanine-substituted mutants of B72 were used to identify the contributions of the selected amino acid residues to the binding to GM1. CD spectra indicated that replacing Lys24, Arg31, and Phe32 with alanine in the B72 peptide did not affect the helical conformation (Figure 7B). The substitution of Arg31 and Phe32 with alanine drastically changed the affinity (Figure 7A and Table 3), which indicates that these residues are essential for GM1's recognition. These residues would be arranged in the C-terminal helix (Figure 1). We previously identified the GM1-binding motif, (W/F)RxL(xP/Px)xFxx(Rx/xR)xP, and the binding of p3 mutants also showed that Arg and hydrophobic residues (Trp and Phe) contributed to the binding (*26*). Polar and aromatic amino acids often play important roles at carbohydrate-binding sites, because carbohydrate−protein interaction is achieved by a combination of hydrophobic interaction and hydrogen bonding (*33*, *43*). The results of alanine scanning were well consistent with our previous results (*26*).

To estimate how much these five amino acids and the helical conformation contribute to formation of the B72−GM1 complex, the Gibbs free energy change (ΔG) upon formation of the complex was calculated from the K_d values. The ΔG values were calculated using the equation $\Delta G = -RT \ln K_d$, where T = 298 K. The difference in ΔG values between the Ct5−GM1 complex (−28.3 kJ/mol) and the B72−GM1 complex (−37.8 kJ/mol) was 9.5 kJ/mol (Figure 8). This energy difference is thought to be due to the five residues, because the only difference between the B72 and Ct5 sequences is these residues. Since the ΔG value of the B72-h−GM1 complex was −30.2 kJ/mol, the distribution of the helical conformation with the presence of the N-terminal half might be estimated to be 7.5 kJ/mol. These energy differences, 9.5 and 7.5 kJ/mol, suggest that both the five residues and the helical conformation were required for the suitable spatial arrangement of five residues on the helix to achieve the specific B72−GM1 interaction.

Table 3: Amounts of Synthetic Peptides Bound to GM1

code	peptide structure [a]	R_{eq} (RU) [b]	relative amount [c]
B72	AELAALEAELAALEGGGGGGGKLKALKRKLRFLKAY-NH_2	261 ± 69	1.0
B72-1	AELAALEAELAALEGGGGGGGKL<u>A</u>ALKRKLRFLKAY-NH_2	130 ± 21	0.50
B72-2	AELAALEAELAALEGGGGGGGKLKALK<u>A</u>KLRFLKAY-NH_2	97 ± 38	0.37
B72-3	AELAALEAELAALEGGGGGGGKLKALKRKL<u>A</u>FLKAY-NH_2	67 ± 3	0.26
B72-4	AELAALEAELAALEGGGGGGGKLKALKRKLR<u>A</u>LKAY-NH_2	54 ± 15	0.21

[a] Alanine substitutions are underlined. [b] The peptide concentration is 5 μM. [c] Ratio to B72.

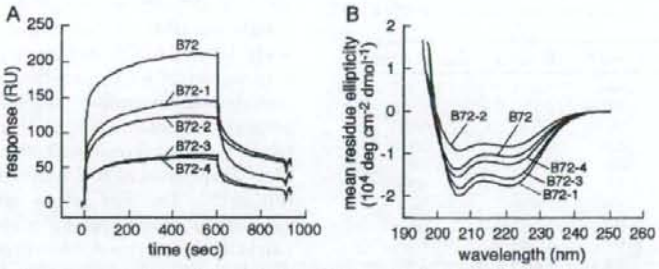

FIGURE 7: Effect of alanine substitutions on the binding of B72 to GM1 and helix formation. (A) SPR sensorgrams for the interaction of B72 and B72 mutants at 10 μM with GM1. (B) CD spectra of B72 and B72 mutants in TBS at pH 7.5. The peptide concentration was 100 μM.

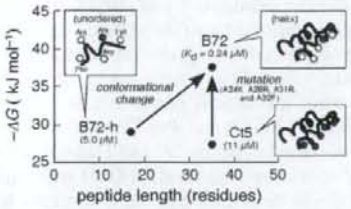

FIGURE 8: Changes in the Gibbs free energy between the complexes of B72, B72-h, and Ct5 with GM1. The ΔG value was calculated from the equation $\Delta G = -RT \ln K_d$, where $T = 298$ K.

B72 exhibited a decrease in the amount bound to asialo GM1 and GM2 (Figure 6), which means that a terminal Gal and Neu5Ac of GM1 are required for the interaction. CTB and p3 also bind to the terminal Gal and Neu5Ac of GM1 (*21*, *22*, *26*). X-ray structural data for the CTB−GM1 complex (Protein Data Bank entry 3CHB) show that the terminal Gal and Neu5Ac interacted with CTB. Therefore, these sugar residues are expected to interact with p3 or B72 in a similar manner. In fact, the binding of CTB to GM1 was competitively replaced with that of B72, and the concentration required for 50% inhibition was 1.1 μM (Supporting Information, Figure S3) (*26*). The molecular modeling shown in Figure 9 indicated that Lys24, Arg28, Arg31, and Phe32 in the C-terminal helix of B72 are arranged to interact with the terminal Gal and Neu5Ac in GM1. A guanidinium group of Arg can form a hydrogen bond with an OH group of the terminal Gal or Neu5Ac and/or salt bridge with a carboxyl group of Neu5Ac. The phenyl group of Phe can form a stack with the hydrophobic B face of the terminal Gal and/or acetoamido group of Neu5Ac.

In conclusion, oligosaccharide-binding peptides with a helix−loop−helix scaffold were selected and their specificities were investigated. One of the peptides exhibited an

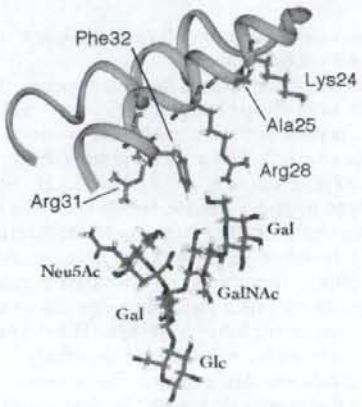

FIGURE 9: Deduced model for the interaction between B72 and pentasaccharide GM1. The side chains of Lys24, Ala25, Arg28, Arg31, and Phe32 in B72 are shown in a stick representation. The GM1 pentasaccharide structure was obtained from Protein Data Bank entry 3CHB.

increase in binding affinity compared with a 15-mer peptide that we identified previously (*26*). The new peptide's helical structure contributed to its ability to recognize carbohydrates, and arginine and phenylalanine were found to be involved in its interaction with GM1. The GM1-binding amino acid residues in the α-helix enabled the peptide to fit GM1. Many antibodies and lectins achieve greater affinity for carbohydrates by displaying carbohydrate-binding residues with a structural scaffold (*33*). This is the first paper to demonstrate the advantages of the arrangement of carbohydrate-binding residues in the helix−loop−helix scaffold for increasing binding affinity.

ACKNOWLEDGMENT

We thank Prof. H. Yanagawa and Dr. N. Doi (Keio University) for providing the opportunity to use the CD spectrometer.

SUPPORTING INFORMATION AVAILABLE

A saturation binding curve of phages to GM1 determined via an ELISA (Figure S1), affinity of phages for various glycolipids (Table S1), amounts of B72 mutant peptides bound to GM1 (Figure S2), and competitive inhibition assay of peptides (Figure S3). This material is available free of charge via the Internet at http://pubs.acs.org.

REFERENCES

1. Varki, A. (1993) Biological roles of oligosaccharides: All of the theories are correct. *Glycobiology 3*, 97–130.
2. Kannagi, R., and Hakomori, S. (2001) A guide to monoclonal antibodies directed to glycotopes. *Adv. Exp. Med. Biol. 491*, 587–630.
3. Qiu, J. X., Kai, M., Padlan, E. A., and Marcus, D. M. (1999) Structure-function studies of an anti-asialo GM1 antibody obtained from a phage display library. *J. Neuroimmunol. 97*, 172–181.
4. Bradbury, A. R., and Marks, J. D. (2004) Antibodies from phage antibody libraries. *J. Immunol. Methods 290*, 29–49.
5. Dinh, Q., Weng, N. P., Kiso, M., Ishida, H., Hasegawa, A., and Marcus, D. M. (1996) High affinity antibodies against Le^a and sialyl Le^a from a phage display library. *J. Immunol. 157*, 732–738.
6. Mao, S., Gao, C., Lo, C. H., Wirsching, P., Wong, C. H., and Janda, K. D. (1999) Phage-display library selection of high-affinity human single-chain antibodies to tumor-associated carbohydrate antigens sialyl $Lewis^x$ and $Lewis^x$. *Proc. Natl. Acad. Sci. U.S.A. 96*, 6953–6958.
7. Wang, L., Radic, M. Z., Siegel, D., Chang, T., Bracy, J., and Galili, U. (1997) Cloning of anti-Gal Fabs from combinatorial phage display libraries: Structural analysis and comparison of Fab expression in pComb3H and pComb8 phage. *Mol. Immunol. 34*, 609–618.
8. Ravn, P., Danielczyk, A., Jensen, K. B., Kristensen, P., Christensen, P. A., Larsen, M., Karsten, U., and Goletz, S. (2004) Multivalent scFv display of phagemid repertoires for the selection of carbohydrate-specific antibodies and its application to the Thomsen-Friedenreich antigen. *J. Mol. Biol. 343*, 985–996.
9. Rojas, G., Talavera, A., Munoz, Y., Rengifo, E., Krengel, U., Angstrom, J., Gavilondo, J., and Moreno, E. (2004) Light-chain shuffling results in successful phage display selection of functional prokaryotic-expressed antibody fragments to N-glycolyl GM3 ganglioside. *J. Immunol. Methods 293*, 71–83.
10. Yamamoto, K., Maruyama, I. N., and Osawa, T. (2000) Cyborg lectins: Novel leguminous lectins with unique specificities. *J. Biochem. 127*, 137–142.
11. Yim, M., Ono, T., and Irimura, T. (2001) Mutated plant lectin library useful to identify different cells. *Proc. Natl. Acad. Sci. U.S.A. 98*, 2222–2225.
12. Yamada, S., Suzuki, Y., Suzuki, T., Le, M. Q., Nidom, C. A., Sakai-Tagawa, Y., Muramoto, Y., Ito, M., Kiso, M., Horimoto, T., Shinya, K., Sawada, T., Usui, T., Murata, T., Lin, Y., Hay, A., Haire, L. F., Stevens, D. J., Russell, R. J., Gamblin, S. J., Skehel, J. J., and Kawaoka, Y. (2006) Haemagglutinin mutations responsible for the binding of H5N1 influenza A viruses to human-type receptors. *Nature 444*, 378–382.
13. Stevens, J., Blixt, O., Tumpey, T. M., Taubenberger, J. K., Paulson, J. C., and Wilson, I. A. (2006) Structure and receptor specificity of the hemagglutinin from an H5N1 influenza virus. *Science 312*, 404–410.
14. DeGrado, W. F., Summa, C. M., Pavone, V., Nastri, F., and Lombardi, A. (1999) De novo design and structural characterization of proteins and metalloproteins. *Annu. Rev. Biochem. 68*, 779–819.
15. Baltzer, L., and Nilsson, J. (2001) Emerging principles of de novo catalyst design. *Curr. Opin. Biotechnol. 12*, 355–360.
16. Bolon, D. N., Voigt, C. A., and Mayo, S. L. (2002) De novo design of biocatalysts. *Curr. Opin. Chem. Biol. 6*, 125–129.
17. Gibas, C., and Subramaniam, S. (1997) Knowledge-based design of a soluble bacteriorhodopsin. *Protein Eng. 10*, 1175–1190.
18. Hosse, R. J., Rothe, A., and Power, B. E. (2006) A new generation of protein display scaffolds for molecular recognition. *Protein Sci. 15*, 14–27.
19. Uchiyama, F., Tanaka, Y., Minari, Y., and Tokui, N. (2005) Designing scaffolds of peptides for phage display libraries. *J. Biosci. Bioeng. 99*, 448–456.
20. Rosinski, J. A., and Atchley, W. R. (1999) Molecular evolution of helix-turn-helix proteins. *J. Mol. Evol. 49*, 301–309.
21. Merritt, E. A., Sarfaty, S., van den Akker, F., L'Hoir, C., Martial, J. A., and Hol, W. G. (1994) Crystal structure of cholera toxin B-pentamer bound to receptor GM1 pentasaccharide. *Protein Sci. 3*, 166–175.
22. Kuziemko, G. M., Stroh, M., and Stevens, R. C. (1996) Cholera toxin binding affinity and specificity for gangliosides determined by surface plasmon resonance. *Biochemistry 35*, 6375–6784.
23. Harder, T., Scheiffele, P., Verkade, P., and Simons, K. (1998) Lipid domain structure of the plasma membrane revealed by patching of membrane components. *J. Cell Biol. 141*, 929–942.
24. Yanagisawa, K. (2007) Role of gangliosides in Alzheimer's disease. *Biochim. Biophys. Acta 1768*, 1943–1951.
25. Matsubara, T., Ishikawa, D., Taki, T., Okahata, Y., and Sato, T. (1999) Selection of ganglioside GM1-binding peptides by using a phage library. *FEBS Lett. 456*, 253–256.
26. Matsubara, T., Iijima, K., Nakamura, M., Taki, T., Okahata, Y., and Sato, T. (2007) Specific Binding of GM1-Binding Peptides to High-Density GM1 in Lipid Membranes. *Langmuir 23*, 708–714.
27. Fujitani, N., Shimizu, H., Matsubara, T., Ohta, T., Komata, Y., Miura, N., Sato, T., and Nishimura, S. (2007) Structural transition of a 15 amino acid residue peptide induced by GM1. *Carbohydr. Res. 342*, 1895–1903.
28. Gram, H., Marconi, L. A., Barbas, C. F., III, Collet, T. A., Lerner, R. A., and Kang, A. S. (1992) In vitro selection and affinity maturation of antibodies from a naive combinatorial immunoglobulin library. *Proc. Natl. Acad. Sci. U.S.A. 89*, 3576–3580.
29. Greenfield, N., and Fasman, G. D. (1969) Computed circular dichroism spectra for the evaluation of protein conformation. *Biochemistry 8*, 4108–4116.
30. Suzuki, N., and Fujii, I. (1999) Optimization of the loop length for folding of a helix loop helix peptide. *Tetrahedron Lett. 40*, 6013–6017.
31. Fujii, I., Takaoka, Y., Suzuki, K., and Tanaka, T. (2001) A conformationally purified α-helical peptide library. *Tetrahedron Lett. 42*, 3323–3325.
32. Rockendorf, N., Bade, S., Hirst, T. R., Gorris, H. H., and Frey, A. (2007) Synthesis of a fluorescent ganglioside G(M1) derivative and screening of a synthetic peptide library for G(M1) binding sequence motifs. *Bioconjugate Chem. 18*, 573–578.
33. Weis, W. I., and Drickamer, K. (1996) Structural basis of lectin-carbohydrate recognition. *Annu. Rev. Biochem. 65*, 441–473.
34. Hyun, S., Kim, J., Kwon, M., and Yu, J. (2007) Selection and syntheses of tentacle type peptides as 'artificial' lectins against various cell-surface carbohydrates. *Bioorg. Med. Chem. 15*, 511–517.
35. Yang, J. T., Wu, C.-S. C., and Martinez, H. M. (1986) Calculation of protein conformation from circular dichroism. *Methods Enzymol. 130*, 208–269.
36. Vila, J. A., Ripoll, D. R., and Scheraga, H. A. (2000) Physical reasons for the unusual α helix stabilization afforded by charged or neutral polar residues in alanine-rich peptides. *Proc. Natl. Acad. Sci. U.S.A. 97*, 13075–13079.
37. Gronow, S., and Brade, H. (2001) Lipopolysaccharide biosynthesis: Which steps do bacteria need to survive? *J. Endotoxin Res. 7*, 3–23.
38. Rudiger, H., and Gabius, H. J. (2001) Plant lectins: Occurrence, biochemistry, functions and applications. *Glycoconjugate J. 18*, 589–613.
39. Love, K. R., and Seeberger, P. H. (2002) Carbohydrate arrays as tools for glycomics. *Angew. Chem., Int. Ed. 41*, 3583–3586.
40. Hirabayashi, J., and Kasai, K. (2002) Separation technologies for glycomics. *J. Chromatogr., B 771*, 67–87.
41. Feizi, T., Fazio, F., Chai, W., and Wong, C. H. (2003) Carbohydrate microarrays: A new set of technologies at the frontiers of glycomics. *Curr. Opin. Struct. Biol. 13*, 637–645.
42. Matsubara, T., and Sato, T. (2007) Identification of oligosaccharide-recognition molecules by phage-display technology. *Trends Glycosci. Glycotechnol. 19*, 121–132.
43. Lis, H., and Sharon, N. (1998) Lectins: Carbohydrate-specific proteins that mediate cellular recognition. *Chem. Rev. 98*, 637–674.

BI8000837

Biochemical and Biophysical Research Communications 371 (2008) 230–235

Contents lists available at ScienceDirect

Biochemical and Biophysical Research Communications

journal homepage: www.elsevier.com/locate/ybbrc

Ganglioside GD1a suppresses TNFα expression via Pkn1 at the transcriptional level in mouse osteosarcoma-derived FBJ cells

Li Wang [a], Yinan Wang [a], Toshinori Sato [b], Sadako Yamagata [a], Tatsuya Yamagata [a,*]

[a] Laboratory of Tumor Biology and Glycobiology, Department of Life Sciences and Biopharmaceutics, Shenyang Pharmaceutical University, P.O. Box 29, 103 WenHua Road, Shenyang, LiaoNing 110016, People's Republic of China
[b] Department of Biosciences and Informatics, Keio University, Hiyoshi, Yokohama 223-8522, Japan

ARTICLE INFO

Article history:
Received 7 April 2008
Available online 22 April 2008

Keywords:
GD1a
TNFα
MMP-9
Cell motility
Pkn1
siRNA
Ganglioside

ABSTRACT

Ganglioside GD1a has been reported to suppress metastasis [S. Hyuga, S. Yamagata, Y. Takatsu, M. Hyuga, H. Nakanishi, K. Furukawa, T. Yamagata, Suppression of FBJ-LL cell adhesion to vitronectin by ganglioside GD1a and loss of metastatic capacity, International J. Cancer. 83 (1999) 685–691.] and MMP-9 production in mouse osteosarcoma FBJ cells [D. Hu, Z. Man, P. Wang, X. Tan, X. Wang, S. Takaku, S. Hyuga, T. Sato, X. Yao, S. Yamagata, T. Yamagata, Ganglioside GD1a negatively regulates MMP9 expression in mouse FBJ cell lines at the transcriptional level, Connect. Tissue Res. 48 (2007) 198–205.]. In the present study, TNFα increased cell motility and MMP-9 and TNFα expression at the transcriptional level. TNFα expression was found to be inversely proportional to GD1a content in the FBJ-cell variants. The addition of exogenous GD1a to FBJ-LL cells suppressed TNFα expression, and treatment of FBJ-S1 cells with D-PDMP (glucosylceramide synthesis inhibitor) led to an increase in TNFα, indicating that TNFα is negatively regulated by GD1a in FBJ cells. SiRNA of Pkn1, a Rho-GTPase effecter protein kinase, suppressed TNFα levels as well as Pkn1 expression, suggesting that Pkn1 is involved in TNFα signaling. Treatment of Pkn1-silenced FBJ-LL cells with GD1a failed to suppress TNFα expression, demonstrating that GD1a signals that lead to TNFα suppression are transduced through Pkn1.

Gangliosides, sialic acid-containing glycosphingolipids, have been demonstrated to have multifarious bioactivity in cells, including roles in immunoreaction and tumor progression [1,2]. The ganglioside GD1a has been demonstrated to regulate metastasis of osteosarcoma FBJ cells [3] possibly through enhancement of caveolin-1 and Stim1 [4] and suppression of MMP-9 [5]. GD1a and GT1b have been shown to induce the production of nitric oxide, tumor necrosis factor alpha (TNFα) and cyclooxygenase-2 in rat brain microglia [6]. GD1a blocks lipopolysaccharide-induced TNFα production and prevents maturation of human dendritic cells [7]. In monocytes, GD1a impairs antitumor immune responses by reducing the release of cytokines IL-6, IL-12, and TNFα [8]. The ganglioside GM3 has been shown to positively regulate TNFα production in mouse melanoma B16 cells with GM3 as the only ganglioside on the cell surface [9], through a PI3K, Rictor/mTOR, Akt, Arhgdib pathway [10].

Tumor necrosis factor alpha (TNFα) is a 17-kDa protein consisting of 157 amino acids, mainly produced by activated macrophages, T lymphocytes, and natural killer (NK) cells. It is a multifunctional cytokine involved in immune reactions, inflammation, cell apoptosis, and survival signals [11]. TNFα is known to work in an autocrine manner through two distinct receptors [12,13]. Secretion of MMP-9 can be enhanced in human vascular smooth muscle cells by stimulation of TNFα [14]. Rho family proteins are involved in TNFα-induced E-selectin and in the extravasation of tumor cells [15], along with TNFα-dependent adhesion of EC cells [16]. The protein kinase Pkn1, a down-stream effecter of Rho-GTPase, has been shown to contain Traf2-binding consensus sequences to activate the NFκB signal pathway [17].

In the present study, we have demonstrated that TNFα secreted by FBJ cells works in an autocrine manner, and is involved in elevated cell motility and MMP-9 secretion of FBJ cells. Expression of TNFα in FBJ cells was found to be negatively regulated by GD1a, and Pkn1 has been shown to be a key molecule in regulating TNFα expression and transducing GD1a signals, thereby leading to the suppression of TNFα in FBJ cells. To the best of our knowledge, this is the first study to show that Pkn1 is involved in ganglioside signals that regulate TNFα signaling and synthesis.

Materials and methods

Cell lines and culture. The highly metastatic mouse osteosarcoma cell line, FBJ-LL, and the poorly metastatic cell line, FBJ-S1, were produced from a FBJ virus-induced osteosarcoma of the BALB/c mouse [18]. LA5-30 cells were obtained by

* Corresponding author. Fax: +86 24 23986433.
E-mail address: tcyamagata@opal.dti.ne.jp (T. Yamagata).

0006-291X/$ - see front matter © 2008 Elsevier Inc. All rights reserved.
doi:10.1016/j.bbrc.2008.04.053

the transfection of FBJ-LL cells with GM2/GD2-synthase; mock-transfected M5 cells were the control [19]. The cells were maintained in RPMI-1640 media as described previously [4].

Chemicals and antibodies. Ganglioside GD1a and GM1 from bovine brain were purchased from Wako (Tokyo, Japan) and Toyobo (Osako, Japan), respectively. Recombinant TNFα was from Sigma (USA), and D-PDMP was from Matreya (USA). Rabbit anti-*p*-serine and rabbit anti-*p*-threonine antibodies were from ZYMED (USA) and CHEMICON (USA), respectively. Mouse anti-β-actin and hamster anti-TNFα antibodies were from Sigma (USA). Mouse anti-Pkn1 antibody was from BD (USA). HRP-linked anti-rabbit and anti-mouse secondary antibodies were from Cell Signaling (USA). POD-affinity anti-Syrian Hamster IgG secondary antibody was from Jackson (USA).

RNA extraction and RT-PCR. RNA extraction and analysis of amplified DNA have been described previously [4]. Primer sequences used for PCR in this study were as follows: for β-actin, sense 5′-ACACTGTGTGCCCATCTACGAGG-3′ and antisense 5′-AGGGGCCGGACTCGTCGTCATACT-3′; for MMP-9, sense 5′-CTGACTACGATAAG GACGGCAA-3′ and antisense 5′-ATACTGGATGCCGTCTATGTCG-3′; for TNFα, sense 5′-TCCAGGCGGTGCCTATGTCT-3′ and antisense 5′-GTTTGAGCTCAGCCCCCTCA-3′; for Pkn1, sense 5′-AGCCTTCAGCGCCATACTGC-3′ and antisense 5′-TGGTCTCGCCAGA ACACAGC-3′.

Construction of a TNFα expression vector. Total RNA was isolated from ascite macrophages of a Balb/c mouse using an RNeasy mini kit (Qiagen) according to the manufacturer's specifications. After first strand cDNA synthesis using TaKaRa RNA LA PCR Kit (AMV) (Takara Bio), a TNFα transcript was amplified using primers: sense, 5′-CAGGGATCCATGAGCACAGAAAGCATGATCCGCGAC-3′ and antisense, 5′-CAGGGATCCTCACAGAGCAATGACTCCAAAGTAGAC-3′. The PCR product was digested with BamHI and inserted into a pIRESpuro3 (Clonetech, USA) vector with puromycin resistance. Transient transfection to FBJ-LL cells was carried out with Fugene reagent (Roche, USA), essentially following the instructions of the manufacturer for mammalian cell transfection. Control cells received an empty vector. Puromycin resistant cells were screened as stable transfectants.

SiRNA and transfection. Selection of target sequences of Pkn1 siRNA was made using a Protein Lounge suggestion and Mulfold software. The target and scrambled sequence were 5′-GCAGGACAGTAAGACCAAGAT-3′ and 5′-TCGCGCTCCACATGATG ACTA-3′, respectively. The sequence was inserted into a retroviral vector with Neomycin resistance at TAKARA Biotechnology Corporation (China). Stable transfection was carried out as described previously [9].

Ganglioside extraction and HPTLC. Cells were grown to ~80% confluence in 10 cm dishes, harvested, and washed three times with PBS(−). Ganglioside extraction and HPTLC were performed as described previously [9].

Wound healing assay. For wound healing assays, monolayered confluent FBJ-LL cells were scraped manually with a pipette tip. Wound size was kept constant to ensure that all wounds had the same width. The cell culture media was replaced with serum-free media containing PBS(-) or TNFα (10 ng/ml). Wound closure was monitored by microscopy and microscopic pictures were taken of more than 10 different areas at 24 h, and number of cells that had moved into the vacant area was scored.

Transwell assay. FBS media (0.6 ml of 0.5%) were placed in the lower wells of a Transwell chamber (Costar, USA). FBJ-LL cells (1×10^5) in 0.1 ml of serum-free media containing PBS(−) or TNFα (10 ng/ml) were placed in each of the upper wells of the chamber. Cells were allowed to migrate for 24 h at 37 °C. Cells that translocated to the lower chamber were counted under the microscope (Nikon inverted TMD microscope, Japan).

Immunoprecipitation and Western blotting. FBJ-LL cells were harvested in a lysis buffer as described previously [4].

Gelatin zymography. FBJ cells were cultured in serum-free media for 12 h and aliquots of conditioned medium were subjected to gelatin zymography analysis, as described previously [20].

Statistical analysis. Data were analyzed using Microsoft Excel. All values are given as mean ± SD and levels of significance are indicated in figures. * indicates significance $P < 0.05$; **, significance $P < 0.01$; and ***, significance $P < 0.001$. NS, not significant.

Results

TNFα is involved in malignant property of FBJ cells and MMP-9 production

We have found that MMP-9 is critical for the migration capability of FBJ cells [20]. Because cytokine TNFα is reported to increase MMP-9 secretion in human vascular smooth muscle cells [14], we then asked if TNFα can affect the motility of FBJ cells. Treatment of FBJ-LL cells that have low levels of GD1a with TNFα (10 ng/ml) for 24 h increased cell motility by approximately 2-fold as judged by wound healing (Fig. 1A) and Transwell experiments (Fig. 1B), implying that TNFα is an important molecule in the malignant properties of FBJ cells.

In order to know whether stimulated motility is related to MMP-9 expression, we cultured several lines of cells in the presence of TNFα (10 ng/ml) for 12 h. The cell lines used in this experiment were: highly metastatic FBJ-LL cells; poorly metastatic FBJ-S1 cells [21]; FBJ-5-30 cells, transfectants that GD1a to the same level as FBJ-S1 cells; and FBJ-M5 cells, the vector control from when FBJ-LL was transfected with GM2/GD2-synthase cDNA [19]. The addition of TNFα to the culture media of any cell line resulted in elevated mRNA synthesis of both MMP-9 (Fig. 1C) and TNFα (Fig. 1D), indicating that MMP-9 and TNFα expression was stimulated by TNFα at the transcriptional level. Aliquots of culture media were subjected to gelatin zymography and the intensity of MMP-9 bands was enhanced by TNFα treatment in each of FBJ cell lines (Fig. 1E). There was no sign of MMP-2 expression in cells treated with TNFα (data not shown).

The induction of MMP-9 by TNFα was further confirmed by transfection of TNFα cDNA into FBJ-LL cells. TNFα levels in stable transfectants were about three times higher than in mock-cDNA-transfected cells. MMP-9 production was also enhanced 3-fold (Fig. 1F). Cell motility of TNFα-transfected cells was highly activated as compared to mock-transfected cells (data not shown), confirming the above results. Taken together, these results clearly demonstrate that TNFα is secreted in an autocrine manner and that TNFα produced in the manner is sure to be involved in elevated cell motility and the production of TNFα and MMP-9.

TNFα is negatively regulated by GD1a in FBJ cells

GD1a has been demonstrated to regulate the metastasis of mouse FBJ-virus-induced osteosarcoma cells [19], possibly through suppression of MMP-9 [5], and in this study, TNFα has been shown to increase MMP-9 secretion. As a result, we were curious about possible regulation of TNFα by GD1a. As revealed by RT-PCR, TNFα expression in FBJ-LL cells was four times higher than in FBJ-S1 cells. This was also the case for FBJ-M5 cells as compared to FBJ-5-30 cells (Fig. 2A and B). Evaluation of TNFα at the protein level (assayed in LL and S1 cells by Western blot) showed that protein levels follow the same patterns as mRNA levels (Fig. 2C and D). GD1a content in FBJ-LL, -S1, M5, and LA5-30 cells (Fig. 2A) shows an inverse relationship between TNFα expression and GD1a content, and suggests that GD1a negatively regulates TNFα in FBJ cells.

Exogenous addition of GD1a (50 μM) to FBJ-LL and FBJ-M5 cells decreased TNFα mRNA levels to a half that of control cells at 12 h (Fig. 3A). Treatment of FBJ-S1 and FBJ-LA5-30 cells with 12.5 μM D-PDMP (an inhibitor of glucosylceramide synthesis) for six days resulted in increased TNFα expression (Fig. 3B) as well as depletion of gangliosides (Fig. 3C). These results clearly support the idea that GD1a negatively regulates TNFα production in FBJ cells. When FBJ-M5 cells were treated with GM1 (50 μM), we found that, besides GD1a, GM1 also decreased TNFα expression (Fig. 3D). In FBJ cells, TNFα augmented TNFα and MMP-9 levels (Fig. 1C and D) that were suppressed in the presence of 50 μM GD1a (Fig. 3E), suggesting that autocrine Tnfα effects are suppressed by GD1a. Taken together, the above results strongly indicate that TNFα expression is negatively regulated by GD1a in FBJ cells.

GD1a down-regulates TNFα expression via Pkn1

In order to identify molecules involved in GD1a signaling during the regulation of TNFα, a protein phosphorylation profile analysis was performed by Kinexus Co. (USA). Among the proteins with altered phosphorylation, a Rho-GTPase associated protein kinases Pkn1 and Pkn2 along with Pdpk1 had enhanced phosphorylation in FBJ-5-30 cells as compared with FBJ-M5 cells (Supplementary Fig. S1). Phosphorylation was measured at serine and threonine residues of Pkn1 isolated from FBJ-LL cells that had been stimu-

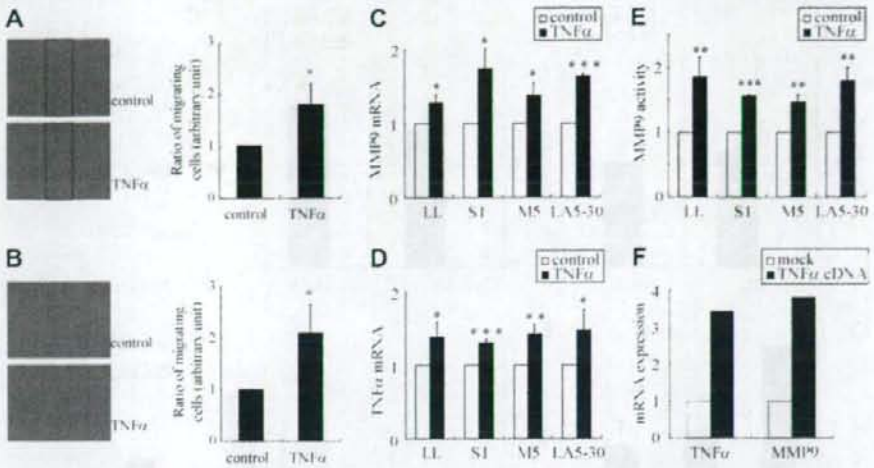

Fig. 1. TNFα stimulated motility of FBJ-LL cells and MMP-9 and TNFα production at the transcriptional level. (A) Wound healing assay of FBJ-LL cells in serum-free RPMI-1640 containing PBS (−) or TNFα (10 ng/ml). (B) Transwell translocation assay using FBJ-LL cells in serum-free media containing PBS (−) or TNFα (10 ng/ml). FBJ cells were treated with TNFα (10 ng/ml) in serum-free media for 12 h, and then total RNA was extracted and subjected to RT-PCR. The amount of MMP-9 or TNFα thus amplified was normalized to β-actin (as a housekeeping gene) and the expression of MMP-9 (C) or TNFα (D) of TNFα treated cells was expressed as the ratio to the control. Conditioned media of FBJ cells that had been incubated in serum-free media with or without TNFα (10 ng/ml) for 12 h was collected and subjected to gelatin zymography (E). FBJ-LL cells were transfected with a TNFα cDNA or with an empty vector (mock), and the expression of TNFα and MMP-9 was determined by RT-PCR (F). The pictures are representative and the data from (A) to (E) are the means of three independent experiments.

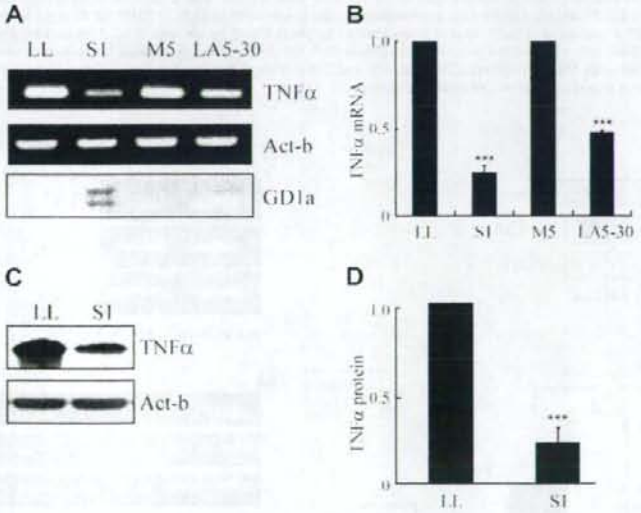

Fig. 2. Inverse relationship of TNFα expression to GD1a content in FBJ cells. mRNA expression of TNFα compared with β-actin in FBJ cells as determined by RT-PCR (A). The bottom panel in (A) represents GD1a content in FBJ cells as revealed by HPTLC. In (B), TNFα expression (normalized to β-actin) in FBJ cells is shown; expression in FBJ-LL cells is set at 1. Cell lysates of FBJ-LL and FBJ-S1 cells were subjected to Western blots to determine expression of TNFα protein levels, with β-actin as an internal control (C). Visualization of panel (C) is given in (D), where TNFα expression in FBJ-LL cells is set at 1. Pictures are representative and the data are the means of three independent experiments.

lated with 50 μM GD1a for 15 min, followed by immunoprecipitation with an anti-Pkn1 antibody. Fig. 4A shows that phosphorylation at serine and threonine residues was enhanced by GD1a stimulation of cells, suggesting that Pkn1 plays a role in GD1a signaling related to TNFα production.

In order to prove that Pkn1 is involved in GD1a signal transduction resulting in suppression of TNFα, polyclonal and monoclonal stable Pkn1 siRNA-transfected cells were obtained; Pkn1 expression was successfully impaired in these cell lines. TNFα expression was suppressed in Pkn1-silenced polyclonal cells (Fig. 4B) and in Pkn1-silenced monoclonal cells (Fig. 4D), suggesting the involvement of Pkn1 in TNFα signaling. The addition of GD1a (50 μM) to the scrambled siRNA-transfected LL cells decreased TNFα expression to similar levels as FBJ-LL cells, while treatment of

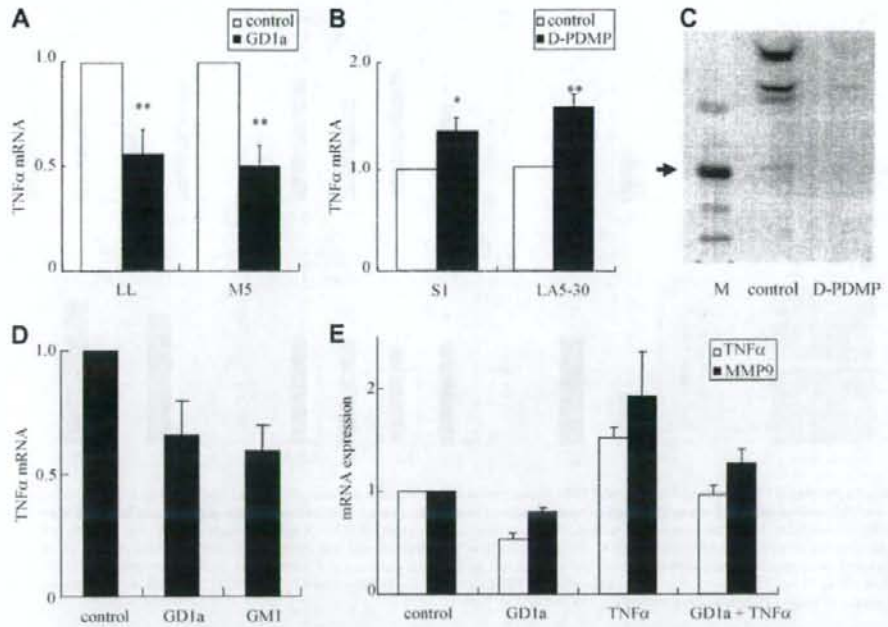

Fig. 3. TNFα was negatively regulated by GD1a in FBJ cells. FBJ-LL and FBJ-M5 cells were treated with GD1a (50 μM) in serum-free media for 12 h, then total RNA was extracted and subject to RT-PCR (A). FBJ-S1 and FBJ-LA5-30 cells were cultured in the presence of 12.5 μM D-PDMP for six days in complete media that was changed every day, then subject to RT-PCR (B). HPTLC pattern of FBJ-LA5-30 cells treated with 12.5 μM D-PDMP for six days in (C). M stands for brain ganglioside mixture, and an arrow shows the position of GD1a. (D), FBJ-M5 cells were treated with GD1a (50 μM) or GM1 (50 μM) in serum-free media for 12 h, and the expression of TNFα was determined by RT-PCR. (E) FBJ-LL cells were treated with TNFα (10 ng/ml), GD1a (50 μM), and TNFα (10 ng/ml) plus GD1a (50 μM) for 12 h, and expression of TNFα and MMP-9 was determined by RT-PCR. The data are the means of three independent experiments.

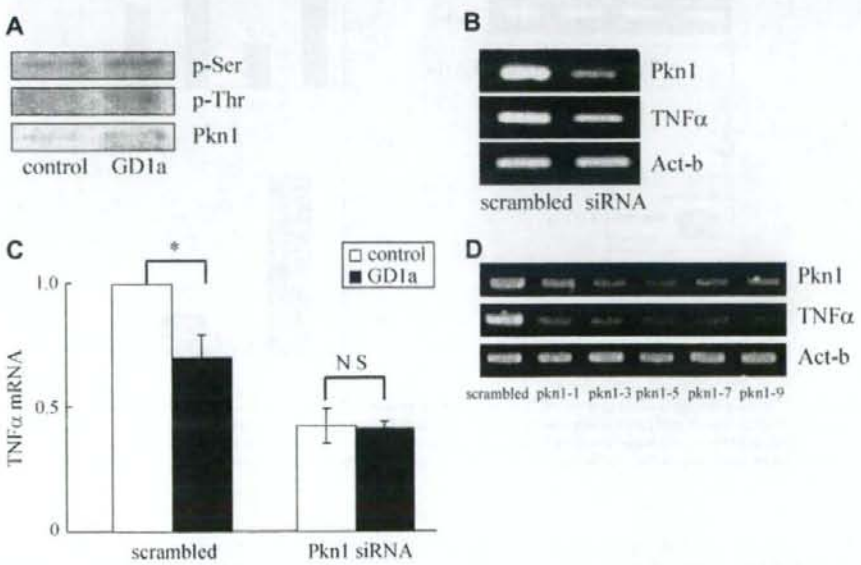

Fig. 4. GD1a suppresses TNFα through Pkn1. Phosphorylation of serine and threonine residues of Pkn1 in FBJ-LL cells that had been stimulated with GD1a (50 μM) for 15 min without serum was determined by immunoprecipitation with Pkn1 antibody, followed by SDS–PAGE and Western blot with the individual phospho-specific antibodies (A). FBJ-LL cells were transfected with either Pkn1 siRNA or scrambled sequence siRNA, followed by selection with G418. Pkn1 and TNFα mRNA expression was determined by RT-PCR with β-actin as a control in polyclonal (B) or in individual monoclonal cells (D). In (C), Pkn1 siRNA or scrambled siRNA-transfected polyclonal cells were incubated with 50 μM GD1a, and TNFα expression was determined by RT-PCR with β-actin as a control. Results are shown with TNFα mRNA of the control cells set to 1. The pictures are representative and the data in (C) are the means of three independent experiments.

Pkn1-silenced polyclonal cells with GD1a failed to reduce TNFα expression (Fig. 4C), distinctly supporting the notion that GD1a signals are transduced to TNFα through Pkn1.

Discussion

GD1a enhances the FBJ-cell expression of caveolin-1 and Stim1 [4], which are known tumor suppressor genes. GD1a suppresses cell motility [3], adhesion to vitronectin [19], and MMP-9 production in FBJ cells [5,20]. In the present study, we have provided evidence that in FBJ cells, TNFα is under the negative control of GD1a via Pkn1. Besides GD1a, ganglioside GM1 also suppressed TNFα expression in M5 cells, indicating that suppression of TNFα by GD1a was not specific to GD1a. The amount of GM1 present in FBJ cells is scant, and its contribution to cell activity may be negligible. SiRNA targeting GD1a-synthase St3gal2 suppressed GD1a production significantly, but did not increase expression of TNFα (data not shown). Since GM1 was as effective as GD1a at decreasing TNFα expression, it is plausible that in the St3gal2 siRNA-transfected cells, GM1 accumulates and functions in place of GD1a. Ganglioside GM3 cannot affect TNFα expression in FBJ cells (data not shown), though GM3 has been reported to positively regulate TNFα at the level of transcription in melanoma B16 cells [9] through the Arhgdib pathway [10]. GD3 was reported to inhibit TNFα induction of MMP-9 via inhibition of p-ERK in human vascular smooth muscle cells [22]. Several lines of evidence imply that the mechanism of regulation of TNFα by gangliosides is not the same in different cell types.

TNFα binds to two different receptors, Tnfrsf1a and Tnfrsf1b [13]. The essential difference between the receptors lies in the death domain of Tnfrsf1a that is absent in Tnfrsf1b. For this reason, Tnfrsf1a can induce apoptosis by recruiting death domain-containing adaptor proteins and activate caspase 8 [23]. In the present study, we have shown that TNFα enhanced FBJ cells motility and cells did not undergo apoptosis (data not shown). It is not clear which TNFα receptors are involved in TNFα signaling in FBJ cells. Research on the mechanism of action of TNFα in FBJ cells is under way in our laboratory.

Since a Kinexus analysis showed that Pkn1 phosphorylation of GD1a-rich FBJ-5-30 cells was activated 3.3 times as high at Thr778 (comparable to Thr774 in human) as GD1a-deficient FBJ-M5 cells (Supplementary Fig. S1), that phosphorylation at Thr774 by Pdpk1 results in Pkn1 activation [24], and we verified that phosphorylation at Thr residues of Pkn1 was high in FBJ-S1 cells than FBJ-LL cells (data not shown), we hypothesized that phosphorylation of Pkn1 in FBJ-LL cells could be activated by GD1a treatment. Phosphorylation at Thr and Ser residues was increased upon GD1a treatment of FBJ-LL cells (Fig. 4). This does not necessarily prove that Pkn1 at Thr778 was phosphorylated by the GD1a signals, but this result is consistent with the analysis of Kinexus and may imply that the GD1a signals have stimulated Pkn1. Pkn1 participation in GD1a signaling will be unambiguously shown if Pkn1 silencing may block the GD1a signals leading to TNFα suppression. Thus, we transfected Pkn1 siRNA into FBJ-LL cells and demonstrated the successful impairment of Pkn1 expression. Pkn1 silencing in FBJ-LL cells significantly lowered TNFα expression, and treatment of these cells with GD1a did not further reduce TNFα expression, whereas treatment of control cells with GD1a notably decreased TNF expression. This result supports the notion that the GD1a signals that lead to TNF suppression go through Pkn1. This is the first paper describing the involvement of Pkn1 in TNF production, and that the GD1a signal is transduced via the Pkn1 pathway. Research to elucidate molecular events up-stream and down-stream of Pkn1 in GD1a-regulated TNFα signals is currently on-going in our laboratory.

Acknowledgment

This work was in part supported by a fund from Mizutani Foundation for Glycoscience (to T.Y.).

Appendix A. Supplementary data

Ganglioside GD1a suppresses TNFα expression via Pkn1 at the transcriptional level in mouse osteosarcoma-derived FBJ cells. Supplementary data associated with this article can be found, in the online version, at doi:10.1016/j.bbrc.2008.04.053.

References

[1] D.M. Marcus, A review of the immunogenic and immunomodulatory properties of glycosphingolipids, Mol. Immunol. 21 (1984) 1083–1091.
[2] S. Hakomori, Tumor malignancy defined by aberrant glycosylation and sphingo (glyco) lipid metabolism, Cancer Res. 56 (1996) 5309–5318.
[3] S. Hyuga, S. Yamagata, T. Tai, T. Yamagata, Inhibition of highly metastatic FBJ-LL cell migration by ganglioside GD1a highly expressed in poorly metastatic FBJ-S1 cells, Biochem. Biophys. Res. Commun. 231 (1997) 340–343.
[4] L. Wang, S. Takaku, P. Wang, D. Hu, S. Hyuga, T. Sato, S. Yamagata, T. Yamagata, Ganglioside GD1a regulation of caveolin-1 and Stim1 expression in mouse FBJ cells: augmented expression of caveolin-1 and Stim1 in cells with increased GD1a content, Glycoconj. J. 23 (2006) 303–315.
[5] D. Hu, Z. Man, P. Wang, X. Tan, X. Wang, S. Takaku, S. Hyuga, T. Sato, X. Yao, S. Yamagata, T. Yamagata, Ganglioside GD1a negatively regulates MMP9 expression in mouse FBJ cell lines at the transcriptional level, Connect. Tissue Res. 48 (2007) 198–205.
[6] H. Pyo, E. Joe, S. Jung, S.H. Lee, I. Jou, Gangliosides activate cultured rat brain microglia, J. Biol. Chem. 274 (1999) 34584–34589.
[7] W. Shen, S. Ladisch, Ganglioside GD1a impedes lipopolysaccharide-induced maturation of human dendritic cells, Cell. Immunol. 220 (2002) 125–133.
[8] S. Caldwell, A. Heitger, W. Shen, Y. Liu, B. Taylor, S. Ladisch, Mechanisms of ganglioside inhibition of APC function, J. Immunol. 171 (2003) 1676–1683.
[9] P. Wang, P. Wu, J. Zhang, T. Sato, S. Yamagata, T. Yamagata, Positive regulation of tumor necrosis factor alpha by ganglioside GM3 through Akt in mouse melanoma B16 cells, Biochem. Biophys. Res. Commun. 356 (2007) 438–443.
[10] P. Wang, X. Yang, P. Wu, J. Zhang, T. Sato, S. Yamagata, T. Yamagata, GM3 signals regulating Tnf-alpha expression are mediated by Rictor and Arhgdib in mouse melanoma B16 cells, Oncology (in press).
[11] R.M. Locksley, N. Killeen, M.J. Lenardo, The TNF and TNF receptor superfamilies: integrating mammalian biology, Cell 104 (2001) 487–501.
[12] J.T. Schroeder, K.L. Chichester, A.P. Bieneman, Toll-like receptor 9 suppression in plasmacytoid dendritic cells after IgE-dependent activation is mediated by autocrine TNF-alpha, J. Allergy Clin. Immunol. 121 (2008) 486–491.
[13] S. Gupta, A decision between life and death during TNFα-induced signaling, J. Clin. Immunol. 22 (2002) 185–194.
[14] S.K. Moon, B.Y. Cha, C.H. Kim, ERK1/2 mediates TNF-alpha induced matrix metalloproteinase-9 expression in human vascular smooth muscle cells via the regulation of NF-kappaB and AP-1: involvement of the Ras dependent pathway, J. Cell. Physiol. 198 (2004) 417–427.
[15] T. Nübel, W. Dippold, H. Kleinert, B. Kaina, G. Fritz, Lovastatin inhibits Rho-regulated expression of E-selectin by TNFalpha and attenuates tumor cell adhesion, FASEB J. 18 (2004) 140–142.
[16] X.L. Chen, Q. Zhang, R. Zhao, X. Ding, P.E. Tummala, R.M. Medford, Rac1 and superoxide are required for the expression of cell adhesion molecules induced by tumor necrosis factor-alpha in endothelial cells, J. Pharmacol. Exp. Ther. 305 (2003) 573–580.
[17] Y. Gotoh, K. Oishi, H. Shibata, A. Yamagiwa, T. Isagawa, T. Nishimura, E. Goyama, M. Takahashi, H. Mukai, Y. Ono, Protein kinase PKN1 associates with TRAF2 and is involved in TRAF2-NF-kappaB signaling pathway, Biochem. Biophys. Res. Commun. 314 (2004) 688–694.
[18] S. Yamagata, M. Miwa, K. Tanaka, T. Yamagata, FBJ virus-induced osteosarcoma has type V collagen consisting of A, B and C-like chains in addition to type I collagen, Biochem. Biophys. Res. Commun. 105 (1982) 1208–1214.
[19] S. Hyuga, S. Yamagata, Y. Takatsu, M. Hyuga, H. Nakanishi, K. Furukawa, T. Yamagata, Suppression of FBJ-LL cell adhesion to vitronectin by ganglioside GD1a and loss of metastatic capacity, Int. J. Cancer 83 (1999) 685–691.
[20] D. Hu, X. Tan, T. Sato, S. Yamagata, T. Yamagata, Apparent suppression of MMP-9 activity by GD1a as determined by gelatin zymography, Biochem. Biophys. Res. Commun. 349 (2006) 426–431.

[21] S. Yamagata, Y. Ito, R. Tanaka, S. Shimizu, Gelatinase of metastatic cell lines of murine colonic carcinoma as detected by substrate-gel electrophoresis, Biochem. Biophys. Res. Commun. 151 (1988) 158–162.
[22] S.K. Moon, S.K. Kang, C.H. Kim, Reactive oxygen species mediates disialoganglioside GD3-induced inhibition of ERK1/2 and matrix metalloproteinase-9 expression in vascular smooth muscle cells, FASEB J. 20 (2006) 1387–1395.
[23] J. Zhou, M. Zhang, S.S. Atherton, Tumor necrosis factor-alpha-induced apoptosis in murine cytomegalovirus retinitis, Invest. Ophthalmol. Vis. Sci. 48 (2007) 1691–1700.
[24] L.Q. Dong, L.R. Landa, M.J. Wick, L. Zhu, H. Mukai, Y. Ono, F. Liu, Phosphorylation of protein kinase N by phosphoinositide-dependent protein kinase-1 mediates insulin signals to the actin cytoskeleton, Proc. Natl. Acad. Sci. USA 97 (2000) 5089–5094.

Biochimica et Biophysica Acta 1778 (2008) 2717–2726

Contents lists available at ScienceDirect

Biochimica et Biophysica Acta

journal homepage: www.elsevier.com/locate/bbamem

Age-dependent high-density clustering of GM1 ganglioside at presynaptic neuritic terminals promotes amyloid β-protein fibrillogenesis

Naoki Yamamoto [a,b,1], Teruhiko Matsubara [c], Toshinori Sato [c], Katsuhiko Yanagisawa [a,*]

[a] Department of Alzheimer's Disease Research, National Institute for Longevity Sciences, National Center for Geriatrics and Gerontology, Obu 474-8522, Japan
[b] Japan Society for the Promotion of Sciences (JSPS), Tokyo 102-8472, Japan
[c] Department of Biosciences and Informatics, Keio University, Yokohama 223-8522, Japan

ARTICLE INFO

Article history:
Received 15 May 2008
Received in revised form 15 July 2008
Accepted 30 July 2008
Available online 7 August 2008

Keywords:
Alzheimer's disease
Amyloid β-protein
GM1 ganglioside
Aging
Synapse

ABSTRACT

The deposition of amyloid β-protein (Aβ) is an invariable feature of Alzheimer's disease (AD); however, the biological mechanism underlying Aβ assembly into fibrils in the brain remains unclear. Here, we show that a high-density cluster of GM1 ganglioside (GM1), which was detected by the specific binding of a novel peptide (p3), appeared selectively on synaptosomes prepared from aged mouse brains. Notably, the synaptosomes bearing the high-density GM1 cluster showed extraordinary potency to induce Aβ assembly, which was suppressed by an antibody specific to GM1-bound Aβ, an endogenous seed for AD amyloid. Together with evidence that Aβ deposition starts at presynaptic terminals in the AD brain and that GM1 levels significantly increase in amyloid-positive synaptosomes prepared from the AD brain, our results suggest that the age-dependent high-density GM1 clustering at presynaptic neuritic terminals is a critical step for Aβ deposition in AD.

1. Introduction

Evidence is accumulating that the interaction of amyloid β-protein (Aβ) with lipid membranes is an early event in its fibril formation in Alzheimer's disease (AD) [1–3]. Previous *in vitro* studies suggested that particular lipid constituents such as cholesterol can be a binding partner for Aβ [4–6]. However, the nature of neuronal membranes responsible for inducing Aβ assembly remains to be determined. We previously identified GM1-ganglioside (GM1)-bound Aβ (GAβ) in the brain that showed early pathological changes associated with AD [7,8]. To date, a number of *in vitro* and *in vivo* studies regarding GAβ have supported the possibility that GAβ acts as an endogenous seed for amyloid fibril formation in the AD brain [9–17]. Yet despite the lines of evidence in favor of this possibility, the GAβ hypothesis has been challenged by a simple question concerning how GAβ is generated in the AD brain.

To explore the mechanism underlying GAβ generation in the brain, we previously examined the lipid composition of synaptosomes prepared from mouse brains at different ages [18]. The prominent findings in that study were as follows. First, the GM1 levels in detergent-resistant membrane microdomains (DRMs) prepared from synaptosomes significantly increased with age and the increase was markedly pronounced in synaptosomes from the human apolipoprotein E4 (apoE4)-knock-in mouse brains compared with those from the apoE3-knock-in mouse brains. Second, the DRMs possessed unique biochemical features distinct from those of lipid rafts; for example, the GM1 accumulation in the DRMs was resistant to methyl-β-cyclodextrin (MβCD) treatment, which is frequently used to destroy cholesterol- and GM1-rich membrane microdomains such as lipid rafts [19,20]. Third, Aβ assembly to amyloid fibril formation was markedly accelerated in the presence of the synaptosomes bearing the DRMs. Together with a previous finding that Aβ deposition likely starts at presynaptic terminals in AD brains [21,22], these findings imply the pathological significance of GM1 accumulation at presynaptic neuritic terminals in AD. Furthermore, this possibility has been supported by a recent study showing that the GM1 levels significantly increase in the amyloid-positive synaptosomes compared with amyloid-free synaptosomes prepared from AD brains [23].

The purpose of this study was to clarify the nature of the GM1-rich, MβCD-resistant DRMs (GMD). Here, we describe that GMD, with a high potency to induce Aβ fibril formation, selectively appeared in synaptosomes but not in non-synaptosomes prepared from mouse brains. Importantly, the synaptosomes bearing the GMD were characterized by their high-density GM1 clustering, which was specifically recognized using a novel peptide (p3; VWRLLAPPFSNRLLP) [24]. Notably, the high-density GM1 clustering in synaptosomes was an age-dependent, and partially, brain-region-specific event. Finally, it was also suggested that sphingomyelin (SM) plays a role in inducing the high-density GM1 clustering in presynaptic plasma membranes.

* Corresponding author. Department of Alzheimer's Disease Research, National Institute for Longevity Sciences, National Center for Geriatrics and Gerontology, 36-3 Gengo, Morioka, Obu 474-8522, Japan. Tel.: +81 562 44 5651x5002; fax: +81 562 44 6594.
E-mail address: katuhiko@nils.go.jp (K. Yanagisawa).
[1] Present affiliation and address: Department of Pharmacy, College of Pharmaceutical Sciences, Ritsumeikan University, Kusatsu 525-8577, Japan.

0005-2736/$ – see front matter © 2008 Elsevier B.V. All rights reserved.
doi:10.1016/j.bbamem.2008.07.028

2. Materials and methods

2.1. Preparation of synaptosomes and non-synaptosomes

Synaptosomes were prepared as previously described [25,26]. A hippocampus or a whole brain minus the hippocampus, cerebellum and brainstem, was homogenized in 0.32 M sucrose buffer containing 0.25 mM EDTA. The homogenate was centrifuged at 580 ×g for 8 min. The supernatant (post-nuclear supernatant) was centrifuged at 14,500 ×g for 20 min. The resulting pellet (crude mitochondrial pellet) was suspended in 0.32 M sucrose buffer without EDTA, layered over Ficoll in sucrose buffer, and then, centrifuged at 87,000 ×g for 30 min. The resultant interface was collected as the source of synaptosomes. On the other hand, the supernatant obtained by the centrifugation of the post-nuclear supernatant was combined with the upper phase obtained by the centrifugation of the suspension of the crude mitochondrial pellet, and then, further centrifuged at 540,000 ×g for 30 min. The resultant pellet was collected as the source of non-synaptosomes.

2.2. Electron microscopy

The synaptosomes isolated from brain homogenates were diluted and then spread on carbon-coated grids, allowing each solution to stand for 2 min before removing excess solution using a filter paper. After drying, the grids were negatively stained with 2% uranyl acetate. Micrographs were obtained by transmission electron microscopy using a JEM-2000EX (JEOL, Tokyo, Japan) with an acceleration voltage of 100 kV.

2.3. Isolation of DRMs

The DRMs were prepared from the synaptosomes and non-synaptosomes according to a previously established method [18]. Briefly, synaptosomes (0.2 mg protein/ml) were homogenized in MES-buffer saline (MBS) containing 1% Triton X-100. The sucrose concentration of the extract was adjusted to 40% by the addition of 80% sucrose in MBS, and then they were overlaid with a 5%/35% discontinuous sucrose gradient in MBS without Triton X-100, followed by centrifugation at 188,000 ×g for 20 h using an SW41-Ti rotor (Beckman, Palo Alto, CA). After centrifugation, 1-ml fractions were harvested from the top to the bottom of the gradient. Success of DRM isolation was verified by confirmation of GM1 enrichment in the fifth fraction as had been reported in our previous study [18].

2.4. SDS-PAGE and Western blotting

The protein concentration of each sample was determined using a BCA protein assay kit (Pierce, Rockford, IL) with bovine serum albumin (BSA) as the standard. The samples were separated by sodium dodecyl sulfate-polyacrylamide gel electrophoresis (SDS-PAGE) and then electrotransferred onto NitroBind membrane (GE Osmonics, Minnetonka, MN). The blots were probed with, monoclonal antibodies specific to SNAP25, syntaxin, nucleaporin p62, aquaporin 4 (AQP4) or CTB-HRP, which were purchased from Stressgen (Victoria, Canada), Santa Cruz (CA, USA), BD Bioscience Pharmingen (CA, USA) Millipore (MA, USA) and SIGMA-Aldrich (MO, USA), respectively. The bands were visualized using an ECL detection system (GE Healthcare, Piscataway, NJ).

2.5. Levels of sphingomyelin, GM1, phospholipids and cholesterol

The sphingomyelin levels in the samples were determined by TLC and scanning densitometry. Lipids were extracted using chloroform/methanol/water 52:26:21 by volume. The lower phase was removed, and the solvent was evaporated and solubilized in chloroform/methanol 70:30 by volume. The lipid extract was spotted onto high-performance TLC plates (Merck, Darmstadt, Germany) and run in three separate solvent systems: methyl acetate/1-propanol/chloroform/methanol/0.25% KCl solution 25:25:25:10:9 by volume; *n*-hexane/diethyl ether/acetic acid 75:23:2 by volume; and *n*-hexane. After each run, the plate was thoroughly dried using hot air. Lipid spots were visualized by dipping the plates in a mixture of 10% $CuSO_4 \cdot 5H_2O$, 8% H_3PO_4, then placing them vertically on paper towels for 1 min to drain the excess charring reagent, followed by heating for 10–20 min at 170 °C. Quantification was performed using NIH image version 1.59 software. The GM1 level in the samples was determined by blot analysis using cholera toxin B subunit-horseradish peroxidase conjugated (CTX-HRP) as previously reported [7]. The cholesterol and phospholipid levels in the samples were determined using Determiner L (Kyowa, Tokyo, Japan) and Phospholipids C (Wako, Osaka, Japan), respectively.

2.6. Aβ incubation in the presence of synaptosomes

Seed-free solutions of Aβ (Aβ1–40) (Peptide Inst., Osaka, Japan) were prepared as previously described [27]. Aβ solutions at 50 μM in Tris-buffered saline (TBS1: 10 mM Tris–HCl and 150 mM NaCl, pH 7.4) were incubated at 37 °C with or without synaptosomes. The fluorescence intensities of Thioflavin T (ThT), which specifically recognizes the amyloid structure, of the mixture incubated for 24 h were determined as previously described [15].

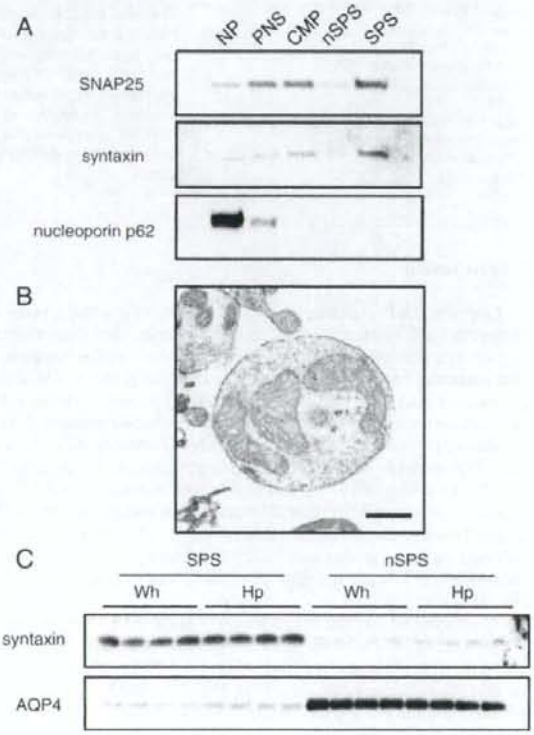

Fig. 1. Characterization of the synaptosomal and non-synaptosomal fractions. (A) Fractions obtained from the preparation of the synaptosomal and non-synaptosomal fractions were subjected to Western blot analysis using monoclonal antibodies specific to SNAP25, syntaxin and nucleoporin p62. (B) The prepared synaptosomes were negatively stained and examined by electron microscopy. Scale bar: 500 nm. (C) The synaptosomal and non-synaptosomal fractions obtained from four animals were subjected to Western blotting assay using monoclonal antibodies specific to syntaxin and AQP4. NP; nuclear pellet, PNS; post-nuclear supernatant, CMP; crude mitochondrial pellet, nSPS; non-synaptosomal fraction, SPS; synaptosomal fraction, Wh: whole brain minus the hippocampus, cerebellum and brainstem, Hp: hippocampus.

2.7. Methyl-β-cyclodextrin (MβCD) treatment

The synaptosomes were washed with Tris-buffered saline (TBS2; 20 mM Tris–HCl, 150 mM NaCl, pH 7.4) at 4 °C and then resuspended in TBS2 with or without 10 mM MβCD. After incubation at 37 °C for 30 min, the mixture was centrifuged at 17,000 ×g for 15 min. The resultant precipitates were subjected to assay or fractionation for DRMs.

2.8. Fluorescence staining of GM1 clustering

Synaptosomes and non-synaptosomes were seeded on poly-L-lysine-coated 24-well plates at a total protein content of 3 μg and incubated either with or without biotin-conjugated p3 (VWRLLAP PFSNRLLP, 300 nM) at room temperature for 1 h. After washing with PBS, the synaptosomes were incubated with Alexa Fluor 594-conjugated streptavidin (10 μg/ml) for 1 h. The synaptosomes incubated alone with Alexa Fluor 594-conjugated streptavidin without p3 treatment did not show labeling.

2.9. Inhibition of membrane-bound neutral sphingomyelinase

PC12 cells were cultured in Dulbecco's modified Eagle's medium (DMEM, Invitrogen, Carlsbad, CA) supplemented with 10% heat-inactivated horse serum and 5% FBS. For their differentiation, PC12 cells were plated on poly-L-lysine-coated (10 mg/ml) chamber slides (Nunc, Roskilde, Denmark) at a density of 50,000 cells/cm^2 and cultured for 6 days in DMEM supplemented with 100 ng/ml nerve growth factor (NGF; Alomone Labs, Jerusalem, Israel). The cells were treated with GW4869 (Calbiochem, Darmstadt, Germany). After 2 days, the cells were fixed with 4% formaldehyde and incubated with 5% BSA blocking agent. The cells were then incubated with biotin-conjugated p3 and Alexa Fluor 488-coupled CTX at room temperature for 1 h. After washing with PBS, the cells were incubated with Alexa Fluor 594-conjugated streptavidin (10 μg/ml) for 1 h.

3. Results

3.1. Characterization of synaptosomes and non-synaptosomes

The isolated synaptosomes were characterized by Western blot analysis using monoclonal antibodies specific to SNAP-25 and syntaxin, which are abundant in presynaptic plasma membrane, and nucleoporin p62, which exclusively localizes at the nuclear membrane [28]. As shown in Fig. 1A, the presynaptic marker proteins were abundant in the synaptosome fractions whereas the nuclear protein was absent in these fractions. Moreover, electron microscopy of the synaptosome fractions revealed typical structural characteristics of synaptosomes with the presence of recognizable mitochondria (Fig. 1B). To compare the characteristics of the isolated synaptosomes and non-synaptosomes, we performed Western blot analysis using monoclonal antibodies specific to syntaxin and AQP4, which is exclusively abundant in astrocyte plasma membrane [29]. As shown in Fig. 1C, the presence of syntaxin and AQP4 in the synaptosomes and non-synaptosomes were mutually exclusive.

3.2. Characterization of GM1 accumulation in synaptosomes

We characterized the GM1 accumulation in synaptosomes and non-synaptosomes using MβCD which can potently break down cholesterol- and GM1-rich DRMs such as lipid rafts by removing cholesterol. Synaptosomes and non-synaptosomes were prepared from whole brain minus hippocampus, cerebellum and the brainstem, and the hippocampus of two different age groups of mice (4-

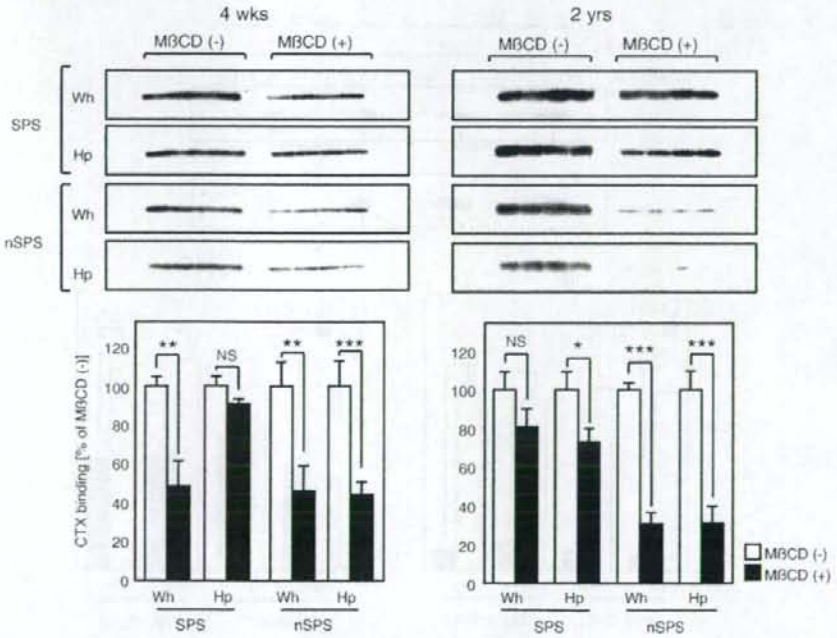

Fig. 2. GM1 accumulates in MβCD-treated synaptosomes prepared from aged mouse brain. The GM1 levels of synaptosomes and non-synaptosomes prepared from young (4-week-old) and aged (2-year-old) mouse brains with or without MβCD treatment are shown. Each lane of the blot contains 1 μg of synaptosomes or non-synaptosome protein prepared from mouse brain. The GM1 levels were determined by densitoscanning the blot following incubation with CTX-HRP. The intensities of the bands relative to those without MβCD treatment are indicated. Each column indicates the average of eight values±S.D. *$p<0.01$, **$p<0.001$, ***$p<0.0001$ (one-way ANOVA combined with Scheffe's test). SPS; synaptosome fraction, nSPS; non-synaptosome fraction, Wh: whole brain minus the hippocampus, cerebellum and brainstem, Hp: hippocampus.

week-old and 2-year-old). The GM1 levels in synaptosomes and non-synaptosomes, which were determined by the specific binding of CTX-HRP, were higher in the samples prepared from aged mouse brains than those from young mouse brains (Fig. 2). Notably, the GM1 accumulation in non-synaptosomes prepared from aged mouse brains markedly decreased following MβCD treatment whereas that in synaptosomes prepared from the same brains was resistant to MβCD treatment (Fig. 2). Although the extent of the GM1 accumulation was lower in the samples prepared from young mouse brains than from aged mouse brains, the resistance of GM1 accumulation to MβCD treatment was consistently observed in synaptosomes prepared from the hippocampus but not from the whole brain (Fig. 2). The levels of cholesterol markedly decreased in synaptosomes and non-synaptosomes from mouse brains of both age groups following MβCD treatment and the decrease in the levels of total phospholipids following MβCD treatment was moderate compared with that of cholesterol (data not shown).

To further characterize the resistance of GM1 showing age-dependent accumulation in the synaptosomes to MβCD treatment, we isolated DRM fractions from the synaptosomes and non-synaptosomes. The successful DRM isolation was confirmed by the observation of GM1 abundance in the fractions as was previously reported (Fig. 3A). We then compared the resistance of GM1 accumulation to MβCD treatment in each fraction between the synaptosomes and non-synaptosomes. Following MβCD treatment, the decrease in GM1 level in the DRM fractions prepared from synaptosomes (arrow a in Fig. 3B) was apparently less than that of the DRM fractions prepared from non-synaptosomes (arrow b in Fig. 3B). MβCD treatment markedly decreased the cholesterol levels, and the levels of total phospholipids also decreased following MβCD treatment but it was less than the decrease in cholesterol levels (Fig. 3B).

3.3. Aβ fibril formation in the presence of the synaptosomes or the DRMs prepared from synaptosomes

We determined whether the GM1 accumulation in the synaptosomes accelerates Aβ assembly into amyloid fibrils. We first incubated soluble Aβ in the presence of the synaptosomes prepared from three different age groups of mice (4-week-old, 1-year-old and 2-year-old groups). The ThT fluorescence intensity in the incubated mixtures increased in an age-dependent manner (Fig. 4A). Notably, the increase in ThT fluorescence intensity was significantly suppressed by coincubation with 4396C, an antibody specific to GAβ, suggesting that amyloid fibril formation in the presence of synaptosomes occurred through GAβ generation. We then incubated soluble Aβ1–40 in the presence of the synaptosomes or non-synaptosomes from aged mouse brain with or without MβCD pretreatment. The ThT fluorescence in

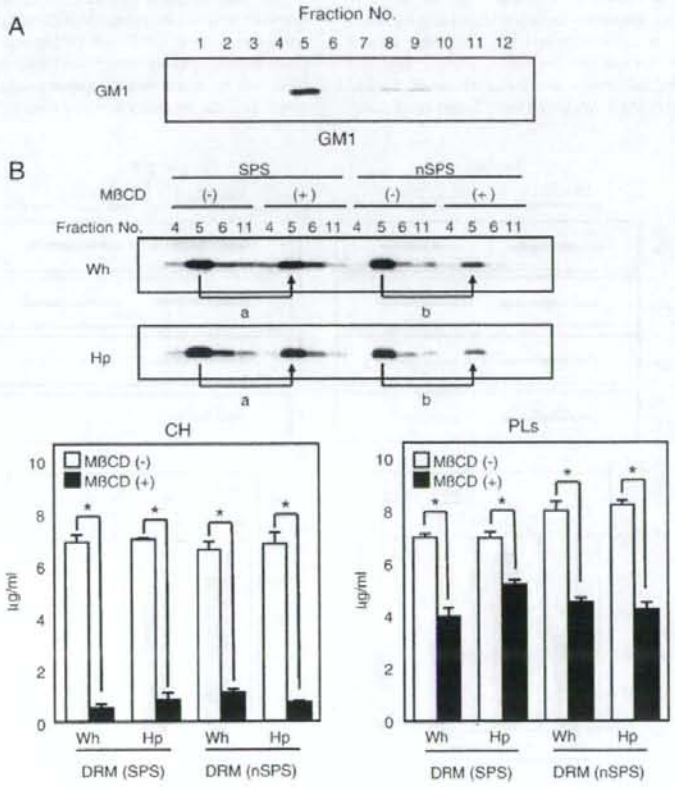

Fig. 3. GM1 accumulates in DRM isolated from MβCD-treated synaptosomes of aged mouse brain. (A) Fractions obtained by DRM isolation through sucrose density gradient fractionation were subjected to blot analysis using CTX-HRP. (B) The blot of DRM isolated from synaptosomes and non-synaptosomes prepared from aged (2-year-old) mouse brain with or without MβCD treatment, which was probed with CTX-HRP, is shown. The cholesterol (CH) and phospholipids (PLs) levels were determined using Determiner L and Phospholipids C, respectively. Each column indicates the average of three values±S.D. *$p<0.0001$ (one-way ANOVA combined with Scheffe's test). SPS; synaptosome fraction, nSPS; non-synaptosome fraction, Wh; whole brain minus the hippocampus, cerebellum and brainstem, Hp; hippocampus.

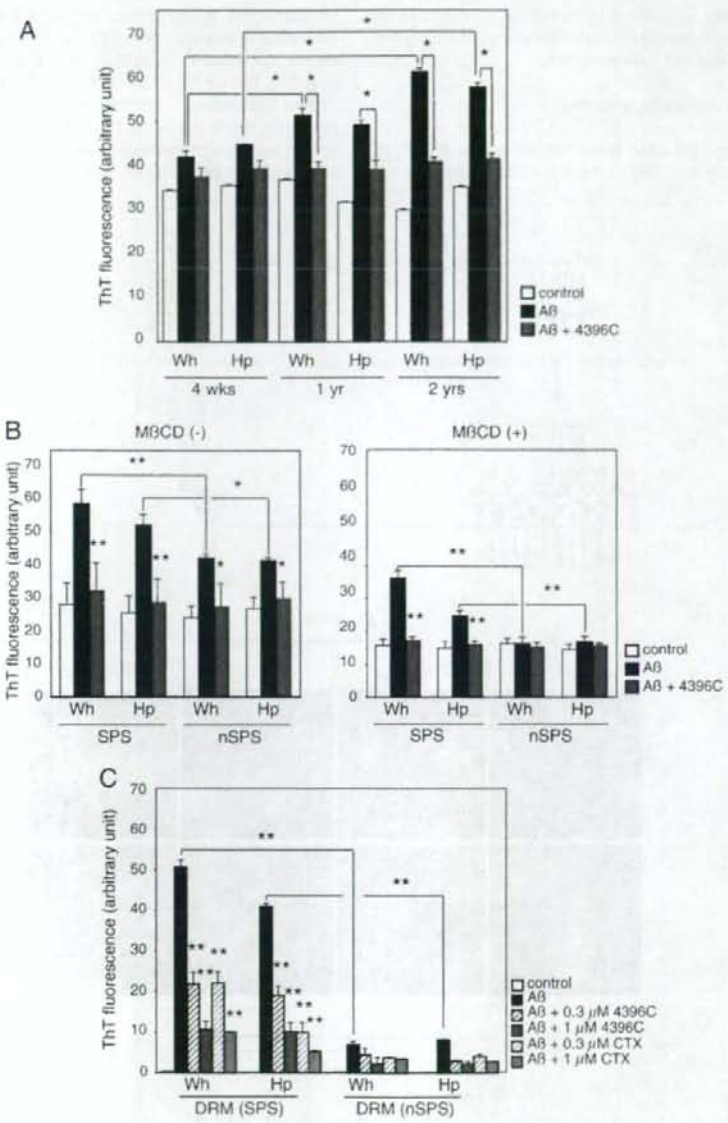

Fig. 4. Aβ assembly in the presence of DRM isolated from synaptosomes of aged mouse brain. (A) The ThT fluorescence intensity of the incubation mixtures containing Aβ incubated at 50 μM and 37 °C for 24 h in the presence or absence of synaptosomes prepared from brains of three different age groups of mice with or without 4396C is shown. (B) The ThT fluorescence intensity of the incubation mixtures containing Aβ incubated at 50 μM and 37 °C for 24 h in the presence or absence of synaptosomes or non-synaptosomes prepared from aged mouse brain with or without 4396C is shown. The synaptosomes and non-synaptosomes had been pretreated with or without MβCD. (C) The ThT fluorescence intensity of the incubation mixtures containing Aβ incubated at 50 μM and 37 °C for 24 in the presence or absence of DRM isolated from synaptosomes or non-synaptosomes of aged mouse brain with or without 4396C or CTX is shown. Each column indicates the average of four values±S.D. *$p<0.001$, **$p<0.0001$ (one-way ANOVA combined with Scheffe's test). SPS; synaptosome fraction, nSPS; non-synaptosome fraction, Wh: whole brain minus the hippocampus, cerebellum and brainstem, Hp: hippocampus.

the incubated mixtures containing the synaptosomes significantly increased compared with that in the incubation mixtures containing non-synaptosomes (Fig. 4B). Again, the increase in the ThT fluorescence intensity was significantly suppressed by coincubation with 4396C. Importantly, the increase in the ThT fluorescence intensity of the incubation mixture was not suppressed by MβCD pretreatment (Fig. 4B).

We then investigated whether the potency of synaptosomes to accelerate Aβ assembly is attributed to the DRMs. We incubated soluble Aβ1–40 in the presence of the isolated DRMs from synaptosomes or non-synaptosomes of aged mouse brain. The ThT fluorescence intensity significantly increased in the incubation mixtures containing the DRMs isolated from synaptosomes but not from non-synaptosomes (Fig. 4C). Again, the increase in the ThT fluorescence

intensity was significantly suppressed by coincubation with CTX or 4396C (Fig. 4C), indicating that amyloid fibril formation in the presence of DRMs is GM1-dependent and GAβ-mediated.

3.4. High-density GM1 clustering on synaptosomes

To further characterize the GM1 accumulation on the surface of synaptosomes, particularly from the viewpoint of GM1 clustering, we incubated the synaptosomes prepared from whole brain and hippocampus of young and aged mouse brains with a novel peptide (p3), which specifically recognizes the high-density GM1 clustering (Fig. 5A). The p3 binding was extremely restricted to synaptosomes and no binding was detected on non-synaptosomes (Fig. 5B). Importantly, the levels of p3 binding to synaptosomes prepared from aged mouse brains was significantly higher than those of p3 binding to synaptosomes prepared from young mouse brains (Fig. 5B, C).

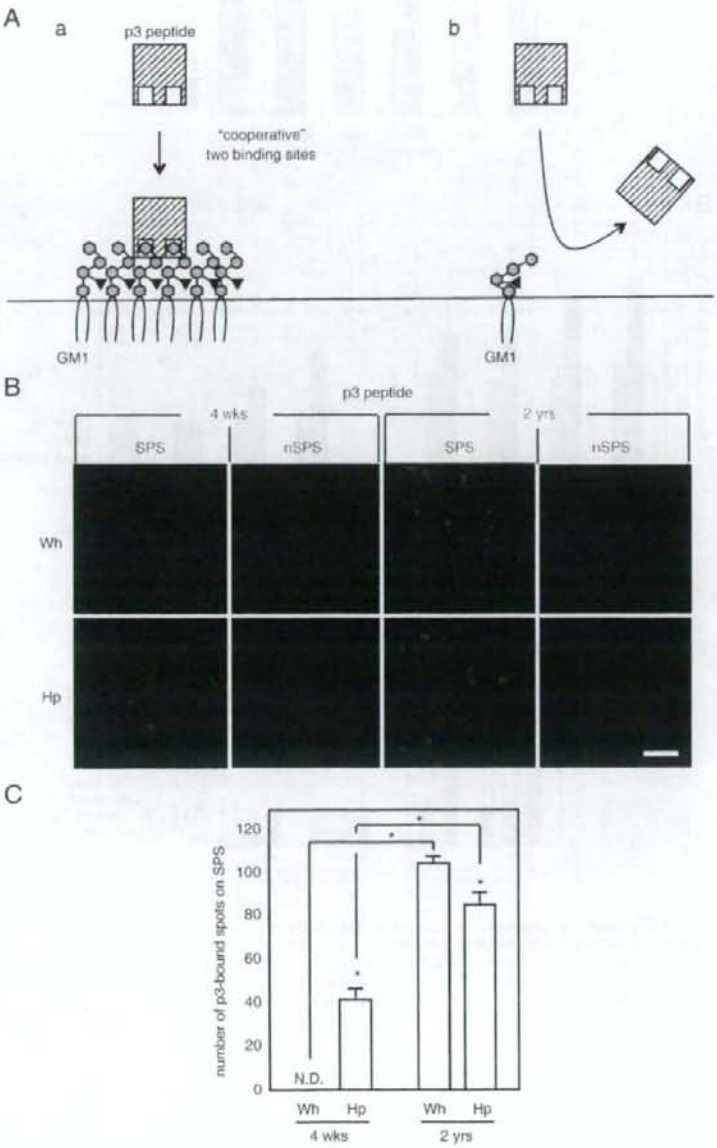

Fig. 5. Peptide p3 binds to synaptosome from aged mouse brain. (A) Proposed scheme for the specific p3 binding to GM1 clusters. (B) The synaptosomes and non-synaptosomes prepared from young (4-week-old) and aged (2-year-old) mouse brains were incubated with biotin-conjugated p3 then with Alexa Fluor 594-conjugated streptavidin. Bar, 50 μm. (C) The number of p3-bound spots shown in (B) was determined. Each column indicates the average of four values ± S.D. *$p<0.0001$ (one-way ANOVA combined with Scheffe's test). ND: not detected. SPS; synaptosome fraction, nSPS; non-synaptosome fraction, Wh: whole brain minus the hippocampus, cerebellum and brainstem, Hp: hippocampus.

Interestingly, in the experiment using synaptosomes obtained from young mouse brains, the p3 binding was only observed in those prepared from hippocampus but not from whole brain (Fig. 5B, C).

3.5. Age-dependent sphingomyelin accumulation in synaptosomes

To explore a possible mechanism of the age-dependent high-density GM1 clustering in synaptosomes, we examined the lipid composition of synaptosomes prepared from three different age groups of mice (4-week-old, 1-year-old and 2-year-old groups). Significantly, the SM levels, which were determined by thin-layer chromatography (TLC), increased with age in synaptosomes prepared from both whole brain and hippocampus (Fig. 6). The GM1 level in synaptosomes also increased with age but to a lesser extent than the increase in SM level, whereas the levels of cholesterol and total phospholipids in synaptosomes remained unchanged, except a decrease in the cholesterol content in the synaptosomes prepared from hippocampus, with age, respectively (Fig. 6). Then, to further characterize the age-dependent SM accumulation in the synaptosomes, we isolated DRMs from the synaptosomes and non-synaptosomes prepared from whole brain minus hippocampus, cerebellum and brainstem, and the hippocampus of aged mouse brains. The SM level was significantly higher in the DRMs isolated from synaptosomes than in those isolated from non-synaptosomes (Fig. 7). Enrichment in the DRMs isolated from synaptosomes was not observed with GM1, cholesterol and total phospholipids (Fig. 7).

3.6. Induction of high-density GM1 clustering at neuritic terminals through sphingomyelinase inhibition

To obtain direct evidence that SM is involved in the induction of high-density GM1 clustering, we incubated PC12 cells, which were induced to differentiate with nerve growth factor, with GW4869, which specifically inhibits plasma-membrane-bound neutral sphingomyelinase (nSMase). The SM levels following nSMase inhibition significantly increased whereas the GM1 levels apparently remained unchanged with the treatment (Fig. 8A). Notably, the p3 binding was specifically observed at neuritic terminals of the PC12 cells, and it was only observed when the cells were pretreated with GW4869. In contrast, the CTX binding at the neuritic terminals was consistently observed regardless of GW4869 pretreatment of the cells (Fig. 8B).

4. Discussion

A previous *in vitro* study using liposomes clearly showed that GM1-mediated Aβ fibril formation through GAβ generation significantly depends on the GM1 distribution but not merely on the GM1

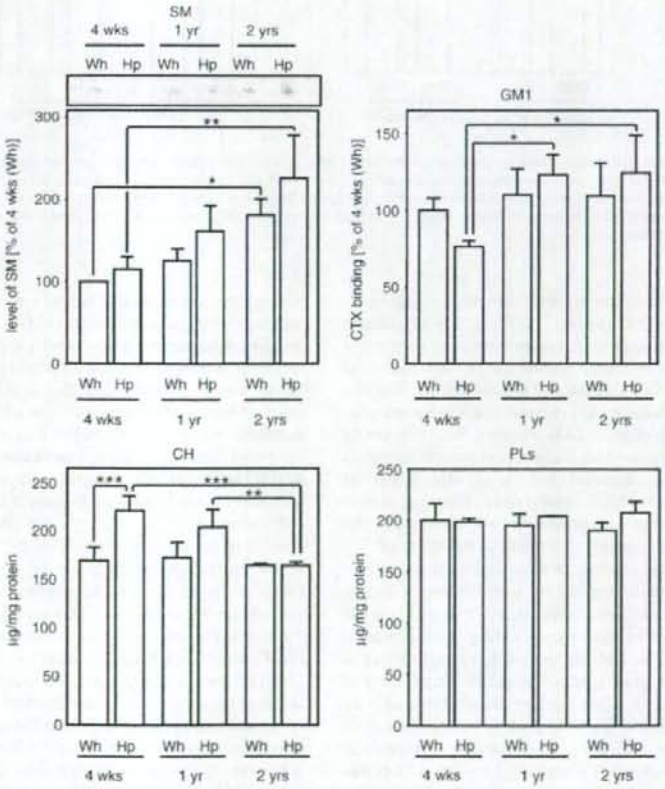

Fig. 6. Aging induces SM and GM1 accumulation in synaptosomes. The lipid composition of synaptosomes prepared from mouse brains of three different age groups is shown. The SM levels were determined by densitoscanning the TLC plate. The intensities of the bands relative to those of the 4-week-old mice are indicated. The GM1 levels were determined by densitoscanning the blot incubated with CTX-HRP. The intensities of the bands relative to those of the 4-week-old mice are indicated. The CH and PLs levels were determined using Determiner L and Phospholipids C, respectively. Each column indicates the average of eight values ± S.D. $^{*}p<0.05$, $^{**}p<0.005$, $^{***}p<0.001$ (one-way ANOVA combined with Scheffe's test). Wh: whole brain minus the hippocampus, cerebellum and brainstem, Hp: hippocampus.

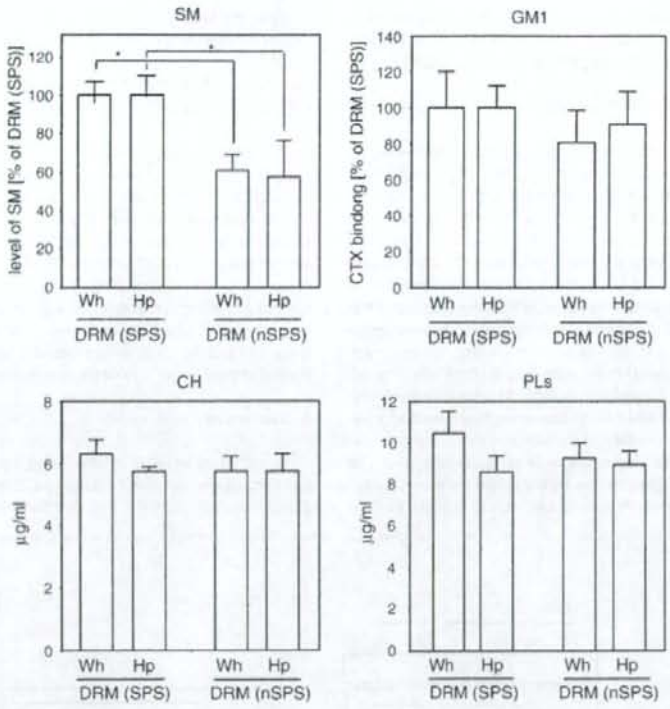

Fig. 7. Lipid composition of DRM isolated from synaptosomes. The lipid composition of DRM isolated from synaptosomes and non-synaptosomes prepared from aged (2-year-old) mouse brain is shown. The SM and GM1 levels were determined by densitoscanning the TLC plate and the blot incubated with CTX-HRP, respectively. The intensities of the bands relative to those of synaptosomes are indicated. The CH and PLs levels were determined using Determiner L and Phospholipids C, respectively. Each column indicates the average of four values ± S.D. *$p<0.001$ (one-way ANOVA combined with Scheffe's test). SPS: synaptosome fraction, nSPS: non-synaptosome fraction, Wh: whole brain minus the hippocampus, cerebellum and brainstem, Hp: hippocampus.

level in the membranes; that is, the Aβ fibril formation is markedly facilitated in the presence of GM1 clusters [13]. Thus, it is a challenge to determine how the GM1 clustering, to the extent that it accelerates GAβ generation, occurs on neuronal membranes under biological conditions. In this study, taking advantage of the specific binding of a novel peptide, p3, to high-density GM1 clusters [24,30], we successfully showed that the high-density GM1 clusters, which potently induce Aβ fibrillogenesis, appeared with age at presynaptic terminals in the brain. This study also suggested that the age-dependent SM accumulation is involved in the high-density GM1 clustering at presynaptic terminals. Our results may provide a new insight into the biological mechanism of Aβ assembly into fibrils in the AD brain.

The novel peptide, p3, has recently been selected from a phage-displayed random peptide library using air–water interface monolayers [24]. From the Hill plot analysis, it was shown that p3 likely has two binding sites that work cooperatively, indicating that the peptide p3 simultaneously binds to two GM1 molecules that stand very close to each other [24]. This is in good contrast to the binding feature of CTX to GM1, where CTX has a single binding site that works non-cooperatively and equally to a single GM1 molecule regardless of its standing whether solitary or in cluster [24]. Although it remains to be clarified how the high-density GM1 clustering provides a favorable microenvironment for GAβ generation, it may be assumed that the alteration of GM1 lateral distribution affects the spatial arrangement of the oligosaccharide chain (head-group) of the GM1 molecule [31].

One of the striking findings of this study is that the high-density GM1 clustering was exclusively observed in synaptosomes but not in non-synaptosomes. To the best of our knowledge, no study has ever compared the lipid composition of DRMs, particularly the GM1 level, between synaptosomes and non-synaptosomes. Further studies are required; however, the GM1 turnover at presynaptic neuritic terminals may be different from that at other neuronal membranes. The result of our recent study is in line with this possibility. That is, the endocytic pathway abnormality that was induced by treatment of PC12 cells with chloroquine, a weak base, facilitated the GM1-induced Aβ fibrillogenesis selectively at presynaptic neuritic terminals [32] regardless of the broad distribution of GM1 throughout the cell body and neurites [33]. Alternatively, the GM1 distribution at presynaptic neuritic terminals may be modified by other membrane constituents. In this context, this study showed that SM preferably localized in the DRMs prepared from synaptosomes compared with in those from non-synaptosomes. It is also interesting to note that the maturation of the axonal plasma membrane is associated with increasing SM levels in DRMs [34]. Furthermore, in terms of the MβCD resistance of the GMD, a previous study suggested that the SM level in a given membrane plays a critical role in the retention of cholesterol against the efflux induced by MβCD [35]. This line of evidence suggests that SM at presynaptic plasma membranes, the level of which increases with age, is involved in the formation of unique membrane microdomains such as the GMD. A previous study also suggested that cholesterol plays a critical role in the formation of GMD, which is responsible for GAβ-induced Aβ assembly [13]. However, we did not observe an age-dependent increase in the cholesterol level in synaptosomes as previously reported [36,37]. At present, the reason for the discrepancy

The fusing ability of sperm is bestowed by CD9-containing vesicles released from eggs in mice

Kenji Miyado*[†‡§], Keiichi Yoshida[‡¶], Kazuo Yamagata[‖], Keiichi Sakakibara*, Masaru Okabe**, Xiaobiao Wang*, Kiyoko Miyamoto*, Hidenori Akutsu*, Takahiko Kondo*, Yuji Takahashi*, Tadanobu Ban[††], Chizuru Ito[¶], Kiyotaka Toshimori[¶], Akihiro Nakamura*, Masahiko Ito*, Mami Miyado*, Eisuke Mekada**, and Akihiro Umezawa*

*National Center for Child Health and Development, 2-10-1 Okura, Setagaya, Tokyo 157-8535, Japan; [†]School of Biomedical Science, Tokyo Medical and Dental University, Yushima, Bunkyo, Tokyo 113-8510, Japan; [¶]Graduate School of Medicine, Chiba University, 1-8-1 Inohana, Chuo-ku, Chiba 260-8670, Japan; [‖]Center for Developmental Biology, RIKEN Kobe Institute, 2-2-3 Minatojima-minamimachi, Chuo-ku, Kobe, Hyogo 650-0047, Japan; and **Research Institute for Microbial Diseases, and [††]Faculty of Medicine, Osaka University, 3-1 Yamadaoka, Suita, Osaka 565-0871, Japan

Edited by Ryuzo Yanagimachi, University of Hawaii, Honolulu, HI, and approved July 8, 2008 (received for review November 8, 2007)

Membrane fusion is an essential step in the encounter of two nuclei from sex cells—sperm and egg—in fertilization. However, aside from the involvement of two molecules, CD9 and Izumo, the mechanism of fusion remains unclear. Here, we show that sperm–egg fusion is mediated by vesicles containing CD9 that are released from the egg and interact with sperm. We demonstrate that the CD9$^{-/-}$ eggs, which have a defective sperm-fusing ability, have impaired release of CD9-containing vesicles. We investigate the fusion-facilitating activity of CD9-containing vesicles by examining the fusion of sperm to CD9$^{-/-}$ eggs with the aid of exogenous CD9-containing vesicles. Moreover, we show, by examining the fusion of sperm to CD9$^{-/-}$ eggs, that hamster eggs have a similar fusing ability as mouse eggs. The CD9-containing vesicle release from unfertilized eggs provides insight into the mechanism required for fusion with sperm.

fertilization | membrane fusion | EGFP | exosome

Fertilization is an essential process that naturally produces a cell capable of developing into a new individual. It consists of sequential events, including membrane fusion of sperm and egg (1). Despite the importance of understanding fertilization in controlling human reproduction and preserving endangered species, the molecular basis underlying the fusion remains a mystery, however. Previously, we reported that a tetraspan-membrane protein (tetraspanin), CD9, is expressed on the egg plasma membrane and is required for sperm–egg fusion (2–4). A role of CD9 in other fusion events also has been demonstrated (5). When sperm are added to eggs from CD9 females, the sperm bind to the egg plasma membrane normally, but fusion is severely impaired (2–4). Two recent observations suggest that CD9 plays a role in the organization of egg membrane. First, CD9 is transferred from the egg to the fertilizing sperm present in the perivitelline space (PVS) (6), suggesting the involvement of a process similar to trogocytosis, a mechanism of cell-to-cell contact-dependent transfer of membrane fragments (7). Second, CD9 deficiency alters the length and density of microvilli on the egg plasma membrane (8). CD9 is also known to be a component of exosomes, membrane vesicles released from a wide range of cells (9, 10). Despite its relationship to CD9, the involvement of exosome release in sperm–egg fusion remains unknown. In the present study, we analyzed the potential of enhanced green fluorescent protein (EGFP)-tagged CD9 (CD9-EGFP) as a reporter protein to study sperm–egg fusion in living mouse eggs.

Results

To observe the movement of CD9 during sperm–egg fusion, we generated a transgenic mouse line that expressed CD9-EGFP only in eggs (Fig. 1*A*), and converted to the genetic background of CD9 mice by mating mice. Western blot analysis using anti-CD9 monoclonal antibody (mAb) revealed that an expected CD9-EGFP with a molecular mass of 51 kDa (CD9 and EGFP

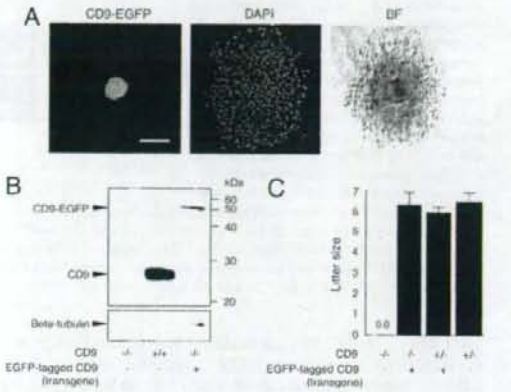

Fig. 1. Generation of mice expressing CD9-EGFP in eggs. (*A*) CD9-EGFP specifically expressed in eggs with mouse ZP3-promoter. Cumulus oocyte complex from Tg CD9$^{-/-}$ oviducts was collected at 14 h after injection of human chorionic gonadotropin. Nuclei of an egg and cumulus cells were counterstained with DAPI. (*Left*) CD9-EGFP. (*Center*) DAPI. (*Right*) Bright field. Scale bar: 100 μm. (*B*) Western blot analysis for eggs collected from CD9 , CD9$^{-/-}$, and Tg CD9$^{-/-}$ mice. The same amounts, including 30 eggs of each lysate, were examined by anti-CD9 and anti-beta-tubulin mAbs (internal control). (*C*) Litter sizes of CD9 (n 31), Tg CD9 (n 35), Tg CD9$^{-/-}$ (n 16), and CD9$^{-/-}$ mice (n 15) (mean SEM). The numbers of females examined are in parentheses.

contributing to 24 and 27 kDa, respectively) was expressed in the eggs collected from Tg CD9 mice; however, the amount of CD9-EGFP expressed in CD9 eggs was estimated to be 10% of that of endogenous CD9 in the CD9 eggs (Fig. 1*B*). Despite the small amount of CD9-EGFP expressed in eggs, CD9-EGFP demonstrated the ability to reverse the sterility of CD9 females (Fig. 1*C*). The numbers of pups obtained from Tg CD9 females (6.4 ± 0.5) were similar to those from

Author contributions: K. Miyado, K. Yamagata, M.O., and A.U. designed research; K. Miyado, K. Yoshida, K.S., X.W., K. Miyamoto, H.A., T.K., Y.T., T.B., C.I., A.N., M.I., and M.M. performed research; K. Miyado contributed new reagents/analytic tools; K. Miyado, K. Yoshida, H.A., K.T., E.M., and A.U. analyzed data; and K. Miyado wrote the paper.

The authors declare no conflicts of interest.

This article is a PNAS Direct Submission.

Freely available online through the PNAS open access option.

[‡]K. Miyado and K. Yoshida contributed equally to this work.

[§]To whom correspondence should be addressed. E-mail: kmiyado@ncch.go.jp.

This article contains supporting information online at www.pnas.org/cgi/content/full/0710608105/DCSupplemental.

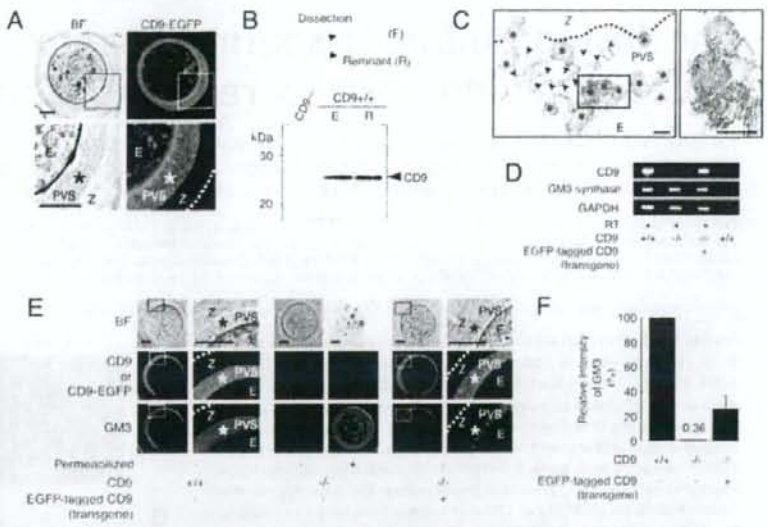

Fig. 2. Identification of secretory vesicles containing CD9 from unfertilized eggs. *A*, A single confocal image showing CD9-EGFP in unfertilized Tg$^+$CD9$^{-/-}$ eggs (E), including the PVS (*), zona pellucida (Z), and the outer margin of the zona pellucida (dotted line). (*Left*) Bright field. (*Right*) CD9-EGFP. *Lower* are enlarged images of the boxed areas. (*B*) Western blot analysis for eggs mechanically fractionated as shown in the diagram: zona-intact CD9$^{+/+}$ eggs (E) (10 eggs per lane) and zona-free CD9$^{+/+}$ eggs (10 eggs per lane). The medium (R) containing the remnant material from 40 eggs treated with a piezo manipulator was loaded in each lane. (*C*) Immunoelectron-microscopic analysis of CD9$^{+/+}$ eggs. The zona-intact CD9$^{+/+}$ eggs were examined using anti-CD9-mAb and 5-nm gold beads conjugated with anti-rat IgG Ab. Left panel: Image including CD9-containing vesicles (*), microvilli (arrowheads), zona pellucida (Z), perivitelline space (PVS), and egg (E). (*Right*) An enlarged image of the boxed region in the left panel. Scale bar: 200 nm. (*D*) RT-PCR for CD9, GM3 synthase, and glyceraldehyde-3-phosphate dehydrogenase transcripts in CD9$^{+/+}$, CD9$^{-/-}$, and Tg$^+$CD9$^{-/-}$ eggs. The same amounts, including 50 eggs in each reaction, were examined. The right end lanes are negative controls in which RT was removed from reactions of wild-type eggs. (*E*) Localization of GM3 and CD9 in CD9$^{+/+}$, CD9$^{-/-}$, and Tg$^+$CD9$^{-/-}$ eggs. (*Left*) Wild-type. (*Middle*) CD9$^{-/-}$. (*Right*) Tg$^+$CD9$^{-/-}$. Right-side of the sets of wild-type and Tg$^+$CD9$^{-/-}$ eggs are enlarged images of the boxed regions. The live eggs were examined, and the internal localization of GM3 in CD9$^{-/-}$ eggs was examined under fixed, permeabilized conditions. (*F*) Comparison of the fluorescent intensities of GM3 stained by antibody in wild-type (n = 10), CD9$^{-/-}$ (n = 9), and Tg$^+$CD9$^{-/-}$ eggs (n = 10) (mean ± SEM). The average values of the wild-type eggs were set to 100%.

Tg$^+$CD9$^{-/-}$ and CD9$^{+/+}$ females (6.0 ± 0.2 and 6.5 ± 0.5) and greater than those from CD9$^{-/-}$ females (0.0 ± 0.0). The CD9$^{-/-}$ females did not exhibit any loss in fertility that could cause a reduction of litter size relative to that of the CD9$^{+/+}$ females (4). Furthermore, the transgene had no effect on normal fertility. These results demonstrate that transgenically expressed CD9-EGFP can compensate for the loss of intrinsic CD9 and yield eggs with the ability to fuse with sperm.

Based on the foregoing evidence, we observed the subcellular localization of CD9-EGFP in "living" Tg CD9$^{-/-}$ eggs (Fig. 2*A*). As expected, confocal microscopic analysis allowed the visualization of two types of CD9-EGFP localization: intense on the plasma membrane and also in the cytoplasm. Unexpectedly, we found loosely filled, noncompacted CD9-EGFP in the PVS, a space formed between the zona pellucida and the plasma membrane of the egg. The localization of CD9 outside the eggs also was confirmed by Western blot analysis using anti-CD9 mAb (Fig. 2*B*). As shown in the diagram, CD9$^{+/+}$ eggs were mechanically fractionated into denuded eggs and other components (R) using a piezo manipulator (11). The fraction R, containing the zona pellucida and the components in the PVS, was centrifuged and subjected to Western blot analysis. The amount of CD9 in the remnant material from 40 eggs was found to be densitometrically equal to that of 10 zona-free eggs, demonstrating an estimated relative abundance of CD9 in the remnant of 20% per egg. Subsequently, we performed immunoelectron-microscopic analysis on the CD9$^{+/+}$ eggs. We identified the vesicles bound to gold particles inside the PVS (Fig. 2*C*). The sectioned microvilli contained a branched network of actin filaments, whereas the variously sized vesicles (50–250 nm in diameter) had uniformly dense materials rather than actin filaments. We also compared CD9$^{+/+}$, Tg CD9$^{-/-}$, and CD9$^{-/-}$ eggs by electron-microscopic analysis [supporting information (SI) Fig. S1]. **The accumulation of vesicles in the PVS in the Tg$^+$CD9$^{-/-}$ eggs was comparable to that in the CD9$^{+/+}$ eggs, whereas it was not seen in the CD9$^{-/-}$ or germinal vesicle-staged CD9$^{+/+}$ eggs. These results indicate that 20% of the total amount of CD9 is stored as vesicles in the PVS during meiosis.**

We next examined the expression of ganglioside GM3, identified as a CD9-associated molecule (12) and a component of exosomes (10), in CD9$^{+/+}$, CD9$^{-/-}$, and Tg$^+$CD9$^{-/-}$ eggs. First, we confirmed the expression of GM3 synthase (ST3GalV/SAT-1) (13) in these eggs by RT-PCR (Fig. 2*D*). Then we investigated the localization of GM3 by immunostaining these live eggs with anti-GM3 mAb (Fig. 2*E*). This antibody has been demonstrated to recognize GM3 in the plasma membrane of cells without treatment for permeabilization (14). Finally, we measured the fluorescent intensities of GM3 in these live eggs (Fig. 2*F*). As expected, in wild-type eggs, GM3 was colocalized with CD9 in the PVS and plasma membrane (Fig. 2*E Left* and Fig. 2*F*). In contrast, in CD9$^{-/-}$ eggs, the fluorescent intensities of GM3 were decreased dramatically in the PVS and plasma membrane (0.4% ± 0.2%, relative to 100% for the CD9$^{+/+}$ eggs), consistent with the loss of CD9 (Fig. 2*E Center* and Fig. 2*F*), whereas GM3 could be detected in the cytoplasm of CD9$^{-/-}$ eggs that had been permeabilized by a detergent after fixation. Moreover, the expression of CD9-EGFP reversed the decrease of GM3 in the PVS and plasma membrane of CD9$^{-/-}$ eggs (25.6 ± 10.7%) (Fig. 2*E Right* and Fig. 2*F*), corresponding to the amount of CD9-EGFP quantified by Western blot analysis (Fig. 1*B*). In addition, electron-microscopic analysis revealed that the number of characteristic membrane structures, termed microvilli (1), were significantly decreased in the CD9$^{-/-}$ eggs compared with the CD9$^{+/+}$ eggs (Fig. S2 *A* and *B*). The numbers of microvilli were increased by ≈50% by the expression of CD9-EGFP in the CD9$^{-/-}$ eggs. The analyses of three types of eggs indicate that CD9- and GM3-containing vesicle release is linked to microvilli formation.

We next investigated the involvement of CD9-containing vesicles in sperm–egg fusion (Fig. 3). We found that, based on the length of microvilli (Fig. S2*C*), zona-intact Tg$^+$CD9$^{-/-}$ eggs can be categorized into two groups (Fig. 3*A*). From single

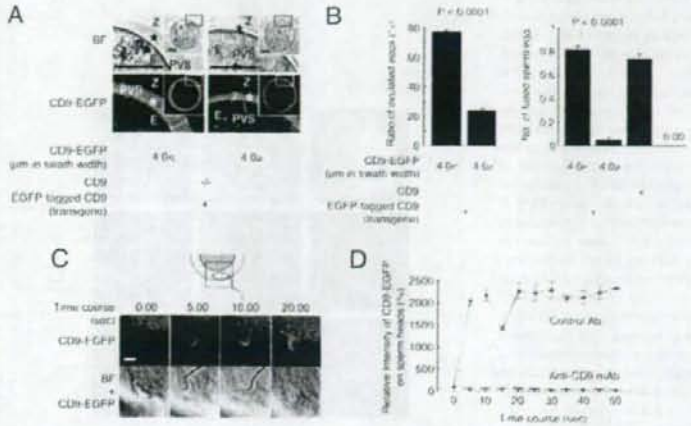

Fig. 3. Involvement of CD9-containing vesicles in sperm–egg fusion. (*A*) Categorization of Tg CD9 eggs (E) into two groups according to the thickness of CD9-EGFP in the PVS (*) and the inner region of the zona pellucida (Z) (4.0 μm or 4.0 μm), indicated by double-headed lines. The boxed regions in *Insets* are enlarged. Scale bar: 20 μm. (*B*) Comparison of the fusing ability of two groups of Tg CD9 eggs with wild-type sperm. Left graph: Ratio of two groups of Tg CD9 eggs ovulated from 12 females (mean SEM). Right graph: Number of sperm fused per egg in two groups of zona-intact Tg CD9 eggs ovulated from 12 females (4.0 μm, *n* 204; 4.0 μm, *n* 66) (mean SEM). CD9 (*n* 120) and CD9 (*n* 112) served as positive and negative controls, respectively. (*C* and *D*) Monitoring of the association of egg CD9-containing vesicles with wild-type sperm. Tg CD9 eggs were incubated with the sperm and monitored immediately after the sperm penetrated the zona pellucida under the presence of anti-CD9 mAb (boxed region). The values were calculated from data scanning by confocal microscopy (15 sperm in triplicate dishes) Blue: Preimmune rat IgG. Red: Anti-CD9 mAb (KMC8) (mean SEM). The average values of the fluorescent intensities of CD9-EGFP at 0 s were set to 100%, and the final concentration of antibodies was adjusted to 50 μg/ml. Scale bar, 5 μm.

confocal images sectioned through the largest diameter, the accumulation of CD9-EGFP from the plasma membrane to the inner region of the zona pellucida was >4.0 μm in swath width in one group and < 4.0 μm in the other group. The accumulation of CD9-EGFP was predicted to show that CD9-containing vesicles are more highly accumulated within the PVS in the >4.0-μm group compared with the < 4.0-μm group. Comparing the ratio of these two groups in Tg CD9 -ovulated eggs revealed a much higher percentage of the >4.0-μm group (77.0 ± 1.3% vs. 23.7 ± 1.5%) (Fig. 3*B Left*). Therefore, we focused on the heterogeneity of CD9-EGFP accumulation within the PVS and determined the ratio of the two groups in zona-intact Tg CD9 eggs that successfully fused with the sperm 6 h after insemination. The >4.0-μm group of Tg CD9 eggs showed higher activity for fusion with sperm (0.81 ± 0.04 sperm fused per egg), compared with the <4.0-μm group of Tg CD9 eggs (0.05 ± 0.03) and the CD9 eggs (0.00 ± 0.00), and comparable activity to that of wild-type eggs (0.73 ± 0.04) (Fig. 3*B Right*). The average activity of all Tg CD9 eggs (0.72 ± 0.03 sperm fused per egg) was equal to that of wild-type eggs (0.73 ± 0.04 sperm fused per egg). The difference between the two groups of Tg CD9 eggs was statistically significant (Fig. 3*B*). These results suggest that the quantities of CD9-containing vesicles, as assessed by the swath width of CD9-EGFP, are strongly correlated with the frequency of sperm–egg fusion.

To detect the association between sperm and CD9-containing vesicles, we serially monitored the wild-type sperm that penetrated the zona pellucida of the Tg CD9 eggs (Fig. 3 *C* and *D*). As shown in the diagram, we began monitoring the sperm immediately after the head portion of sperm penetrated the zona pellucida of the Tg CD9 eggs (Fig. 3*C Upper*, boxed area in the diagram). Soon after we began to monitor the sperm, the fluorescent intensities of CD9-EGFP on the sperm heads increased and then decreased rapidly between 0 s and 15 s, then increased again, reaching a maximum at 20 s. At this point, the CD9-EGFP fully covered the surface of the sperm heads. In contrast, when the sperm were incubated with Tg CD9 eggs in the medium containing anti-CD9 mAb, no increase in intensity of CD9-EGFP on the sperm heads was detected. Anti-CD9 mAbs have been reported to inhibit sperm–egg fusion (4, 15, 16). Our findings demonstrate that the anti-CD9 mAb inhibited the association of sperm with CD9-containing vesicles in parallel to inhibition of sperm–egg fusion.

To determine whether CD9-containing vesicles are capable of initiating sperm–egg fusion, we incubated the sperm with CD9 eggs in medium containing the vesicles collected from CD9 eggs (Fig. 4 and Fig. S3). To restrict the source of CD9 into the vesicles from the CD9$^{+/+}$ eggs, we used sperm collected from the epididymis of CD9$^{-/-}$ males. We estimated the capability of the vesicles to influence fusion by counting the number of sperm fused with CD9$^{-/-}$ eggs. As shown in the experimental design, after the zona pellucida was removed from the CD9$^{-/-}$ eggs, the eggs were incubated with sperm in the medium containing the vesicles (Fig. 4*A*). When examined at 1 h after incubation, the sperm were seen to be capable of fusing with CD9$^{-/-}$ eggs after co-incubation with the vesicles (Fig. 4*A Center*), indicating restoration of the fusibility of CD9$^{-/-}$ eggs with the sperm (0.58 ± 0.07 sperm fused per egg) (Fig. 4*B*). We detected further evidence of sperm–egg fusion in the CD9$^{-/-}$ eggs from which a second polar body had been extruded. In contrast, we did not detect improved fusibility of sperm with eggs in medium depleted of CD9-containing vesicles using beads conjugated with anti-CD9 mAb (Fig. 4*A Right* and *B*). After treatment with the beads, the quantity of CD9 in the depleted medium was significantly decreased, to 16% of the untreated medium (Fig. 4*C*). In addition, CD9$^{-/-}$ remnants failed to rescue the fusing ability of CD9$^{-/-}$ eggs. These findings indicate that the association with CD9-containing vesicles renders the sperm capable of fusing with eggs without endogenous CD9 expression. We estimated the relative abundance of CD9 in the remnant as 18% of the total amount in the eggs (Fig. 4*C*). We further found